On the Behavior of Pliable Plate Dynamics in Wind: Application to Vertical Axis Wind Turbines

Thesis by

Julia Theresa Cossé

In Partial Fulfillment of the Requirements

for the Degree of

Doctor of Philosophy

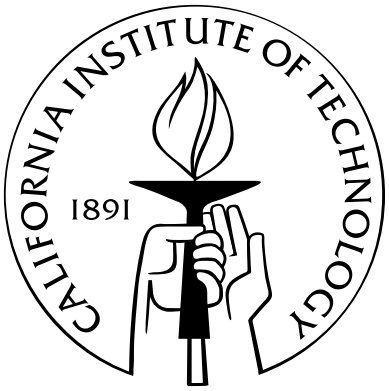

California Institute of Technology

Pasadena, California

2014

(Defended April 22, 2014)

In memory of Zachary Weston

Acknowledgements

This body of work would not have been possible without the help and insight of many individuals. I would like to thank my adviser, Mory Gharib, for all of his advice, support and wisdom throughout my time at Caltech. I am also tremendously grateful to all of my committee members: John Sader, for his collaboration, development of theory included in Chapter 4, guidance, and constant enthusiasm; John Dabiri, for the relentless optimism, support, and advice; and Beverley McKeon, for the continuous support and encouragement during my years at Caltech.

In addition, I would like to thank the Gharib group members past and present for their help and support; in particular, Daegyoum Kim and Cecilia Huertas Cerdeira for their contributions to the inverted flag studies, and Lutz Mueller for his help designing and managing the fabrication process for the VAWT prototype at the field. I am also grateful to Bob Hayes, the rest of the team at Prevailing Wind Power, Matthias Kinzel, and the Dabiri lab group, who all helped and supported the experimental efforts at the Caltech Field Laboratory for Optimized Wind Energy. I want to thank David Kremmers for the inspiring and illuminating conversations. In addition, I'm grateful to Mitul Luhar for the helpful conversations, insight, and support implementing the reconfiguration model to the flexible bladed VAWT.

I would also like to thank GALCIT and LADHYX for the opportunity to participate in the Caltech - Ecole Polytechnique exchange program. In particular, I'm grateful to Emmanuel de Langre for inspiring my interest in fluid-structure interactions. I am grateful to the Keck Institute for Space Studies for supplying funding for my first year at GALCIT, as well as the Moore Foundation for providing the funding for my research.

Last, but not least, I am incredibly grateful to all of my family and friends for their constant support and encouragement throughout my entire education.

Abstract

Numerous studies have shown that flexible materials improve resilience and durability of a structure. Several studies have investigated the behavior of elastic plates under the influence of a free stream, such as studies of the fluttering flag and others of shape reconfiguration, due to a free stream.

The principle engineering contribution of this thesis is the design and development of a vertical axis wind turbine that features pliable blades which undergo various modes of behavior, ultimately leading to rotational propulsion of the turbine. The wind turbine design was tested in a wind tunnel and at the Caltech Laboratory for Optimized Wind Energy. Ultimately, the flexible blade vertical axis wind turbine proved to be an effective way of harnessing the power of the wind.

In addition, this body of work builds on the current knowledge of elastic cantilever plates in a free stream flow by investigating the inverted flag. While previous studies have focused on the fluid structure interaction of a free stream on elastic cantilever plates, none had studied the plate configuration where the trailing edge was clamped, leaving the leading edge free to move. Furthermore, the studies presented in this thesis establish the geometric boundaries of where the large-amplitude flapping occurs.

Contents

List of Figures

List of Tables

Chapter 1

Introduction

"Perhaps the sharpest contrast in mechanical design between the larger products of natural selection and those of human contrivance is in stiffness. We find relatively rigid structures comfortable to manufacture and use while nature seems to make better and more extensive use of more flexible materials and structures." Vogel (1984)

Vogel has repeatedly pointed out nature's use of flexibility as an interesting area of study. His work has investigated the reconfiguration of leaves due to wind (Vogel (1984, 1989); Etnier and Vogel (2000)). Moreover, Vogel points out humanity's aversion to flexible structures. The example of flight demonstrates our relative comfort with stiff materials. Man-made planes with rigid wings and jet engines separate lift and thrust functions, while nature utilizes a flapping pliable wing responsible for both lift and thrust.

This thesis presents a rigorous investigation of the large spectrum of behavior exhibited by elastic cantilever plates and the application of such plates to a vertical axis wind turbine (VAWT). A VAWT was designed to use pliable blades in order to improve energy harvesting and durability characteristics. Wind tunnel testing showed that the VAWT with pliable blades could self-start and produce power. Unexpectedly, large-amplitude flapping was observed during these initial tests, which lead to the discovery of a new flapping plate instability. The study progressed in two directions: one was a more rigorous investigation of elastic cantilever plates; the second was the

further development of the VAWT design, including building and testing a full-scale prototype at the Caltech Field Laboratory for Optimized Wind energy.

1.1 Background

1.1.1 Vertical Axis Wind Turbines

In recent years vertical axis wind turbine arrays have been shown to produce more power per unit land area than horizontal axis wind turbines, primarily due to the difference in spacing requirements between the two turbine types (Dabiri (2011) and Kinzel et al. (2012)). While vertical axis wind turbines (VAWTs) were the first type of wind turbine in existence (Hau (2006)), horizontal axis wind turbines (HAWTs) quickly became the prevailing wind energy converter due to their higher efficiency. The result of this shift in focus is that horizontal axis wind turbines have gone through many more years of technical development than their counterparts. Consequently, vertical axis wind turbines have remained an immature technology (Hau (2006)).

One significant difference between VAWTs and HAWTs is the method with which the blades interact with the wind. HAWTs orientate their rotor blades perpendicular to the wind, i.e. their power production depends on the angle between the wind direction and the rotor. With proper alignment between wind direction and the rotor, the blades continuously produce lift, which in turn keeps the rotor spinning. In contrast, VAWTs are independent of wind direction. The blades must produce positive torque throughout half of one rotation, while minimizing any negative impact on rotor rotation as the blades are carried back upstream. This is due to the symmetry of the turbine as laid out in Figure 1.1, where a VAWT is depicted from the side (a) and from above (b). Notably, the blade aerodynamics change dramatically over the course of a rotation because the angle of attack changes due to the rotation.

Historically, creating the necessary torque differential has been solved in two ways: the first solution was to build a wall in front of the negative torque region, preventing any forces from wind occurring on this half of the turbine (see Figure 1.2b); the

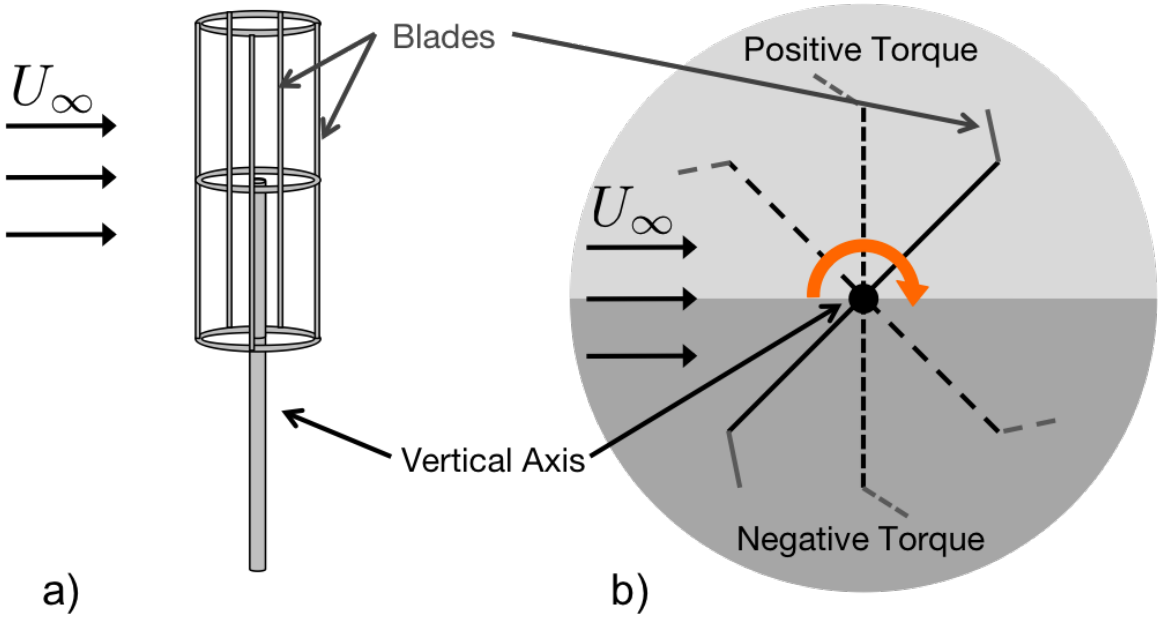

Figure 1.1. Birds eye view of a vertical axis turbine, showing the need for one side of the turbine to produce a higher torque than the other in order to produce rotation.

second solution was to create non-symmetric blade shapes. This concept can be further divided into two categories: air foils in the case of lift-driven Darrieus rotors, or bucket-like scoops in the case of drag-driven Savonius rotors, shown in Figure 1.2c (Sheldahl et al. (1977)). However, both of these solutions involve compromises. In the case of building a wall to create flow blockage, the benefit VAWTs exhibit over HAWTs of being directionally independent of the wind direction is removed by the large wall structure forcing directional dependence. In the second case of non-symmetric blades, manufacturing complication, and thus additional expense, creates a suboptimal solution.

Mechanisms to prevent damage during storms are also important elements of wind turbine design. HAWTs have many mechanisms to prevent damage caused by high winds. They can either rotate the entire rotor section parallel to the wind or change the pitch of the blades to avoid over-spinning. In contrast, VAWTs have relied on both mechanical and electrical breaks to prevent the turbine rotor from spinning too fast.

This body of work explores the simple solution of using flat, rectangular sheets

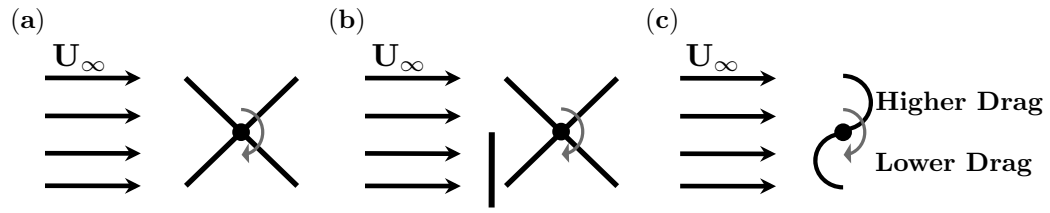

Figure 1.2. Geometry of vertical axis wind turbine designs as viewed from above the turbines. Figure 1.2a shows a VAWT with perfect symmetry, which is therefore unable to rotate. Figure 1.2b shows the use of a wall in front of half the turbine to impose the force differential needed for rotation, while Figure 1.2c shows a Savonius turbine, which uses geometric differences to break the symmetry of forces acting on the blades.

of pliable materials as the blades of a VAWT. The idea sprang from the drag enhancement as well as drag reduction qualities of shape reconfiguration. Vogel (1984) and Cossé (2010) noted that pliable structures have both drag enhancing and drag reducing properties, dependent only on the angle of attack of the blade relative to its clamp and fluid flow direction. The principle was incorporated in a turbine design, which used reconfiguration to produce a torque differential across the turbine. The positive torque side would use drag enhancement, while the negative torque side would minimize forces acting on the turbine by utilizing the drag reduction.

1.1.2 Fluid Structure Interaction of Cantilever Plates

Fluids moving over elastic plates, and the resultant motion of the plate, have previously been studied in several contexts. These studies can be separated into groups based on the boundary conditions of the plate with respect to the flow. Considering that, this thesis develops and uses a pictorial representation of the boundary conditions. An example of the pictorial representation is shown in Figure 1.3. The orange block represents the clamped interface of the plate, indicating whether the plate follows or precedes the clamp in relation to the direction of the free stream. In this 2D representation, only the edge of the plate is observed, as its width extends into the page. The direction of gravity is indicated, either with an arrow, or alternatively by a circle when gravity points into the page.

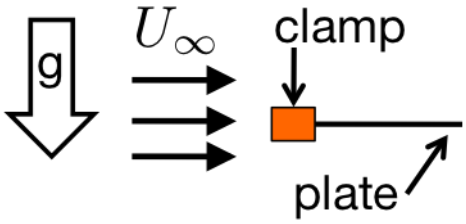

Figure 1.3. Pictorial representation of boundary conditions.

1.1.2.1 Fluttering Flag

The fluttering flag is shown pictorially in Figure 1.4. Experiments have investigated different flag orientations with respect to gravity, each observing flutter above a critical wind speed (Taneda (1968)). Kornecki et al. (1976) rigorously developed the

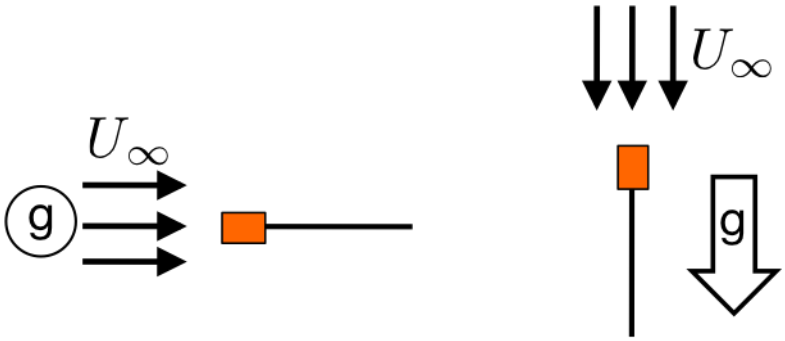

Figure 1.4. Fluttering Flag Configurations

governing equations for the plate movement. Two modes of plate instability were established: static (divergence) or dynamic (flutter), depending on the boundary conditions and flow speed (Kornecki et al. (1976)).

Experimental studies of the fluttering flag are numerous. Examples include Zhang et al. (2000), who studied silk thread in soap films. Shelley et al. (2005) investigated the effect of mass ratio in water, adding weights to the flag. Eloy et al. (2008) studied a streamlined mast, clamping the flag at the leading edge. Hœpffner and Naka (2011) investigated the 3D nature of the flapping waves observed in the flag due to gravity. Ristroph and Zhang (2008) studied the interaction between and array of multiple flapping flags.

1.1.2.2 Reconfiguration

Fluttering flags are not the only area of study investigating elastic cantilever plates. Reconfiguration is the term given to deformation due to the drag of a moving fluid. Figure 1.5 shows the different boundary conditions where reconfiguration has been observed.

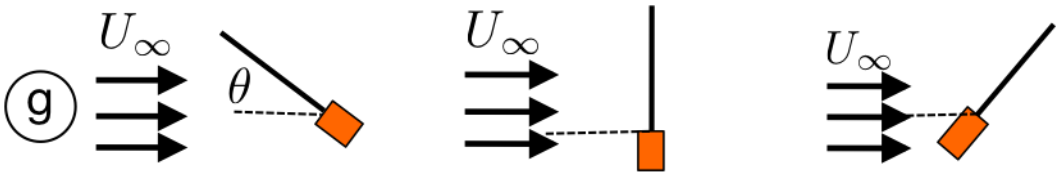

Figure 1.5. Reconfiguration

Vogel (1984) focuses purely on the behavior of flexible plants when experiencing drag from the wind and how this behavior differs from rigid structures. In addition, Vogel (1984) recognizes that such shape morphing behavior can occur during time scales as short as a wind gust. He goes on to study reconfiguration of leaves and the declining drag exerted on leaves (see Vogel (1989)). These works led to many studies of plants both in air and water exhibiting similar behavior.

Gosselin et al. (2010) propose a scaling relationship which successfully collapses the relationship between drag and reconfiguration for a large number of prior studies. Luhar and Nepf (2011) extend this theory by including the effects of buoyancy for water based flows. The focus in all of these studies is on drag reduction and not on reversing the phenomena to drag enhancement. Two studies show that drag enhancement is also possible. Vogel (1984) mentions an initial increase in drag due to reorganization of leaves at low speeds, which was confirmed experimentally and through scaling relationships by Cossé (2010) to depend on the initial angle of the body with respect to the free steam.

1.1.2.3 Inverted Flag Orientation

The fully inverted orientation, shown in Figure 1.6, was considered in a few preceding studies. However, in these studies, other geometric factors prevented the occurrence of the dramatic large-amplitude oscillations that are investigated in this thesis (Etnier and Vogel (2000); P. Buchak and Reis (2010); Rinaldi and Paidoussis (2012)).

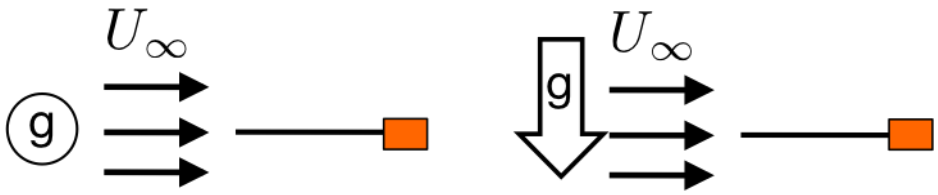

Figure 1.6. Inverted Flag Configuration

Etnier and Vogel (2000) may have been the first to study an inverted orientation of a flexible body, in the form of a daffodil flower. The flower was observed to reconfigure away from the wind, twisting around its stem. Two other studies, P. Buchak and Reis (2010) and Rinaldi and Paidoussis (2012), study the inverted behavior of low aspect ratio plates. This work will show that the large-amplitude flapping discussed in Chapter 4 doesn't occur at such low aspect ratios. Kim et al. (2013) shows that the large-amplitude flapping is associated with an increase in drag coefficient.

This thesis will show that the concept of a VAWT with reconfiguring rotor blades proved successful in achieving the torque differential necessary for power production in both wind tunnel and field tests. Figure 1.7 shows the full range of boundary conditions relevant to the vertical axis turbine design discussed in this thesis. Unexpectedly, blades flapped violently during some of these boundary conditions. Further investigations revealed a large-amplitude flapping instability (Kim et al. (2013)). In order to understand the VAWT blade behavior, a thorough study of an elastic plate with inverted boundary conditions (Figure 1.7a-b) was conducted. Finally, a full scale VAWT was tested at the field site.

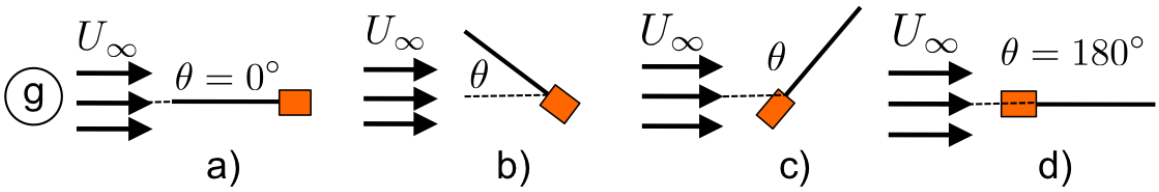

Figure 1.7. There are several different orientations with which the plate, clamp and fluid flow can interact. The four orientations displayed result in very different behaviors from each other.

1.2 Study Objectives

The principal goal of this thesis is to prove the hypothesis that pliable blades can create the drag differential necessary for a vertical axis wind turbine to convert wind to electrical energy. The accompanying goals include providing physical explanations to the blade behavior observed, while broadening our understanding of fluid-structure interactions.

(a) To prove passive blade deformation is sufficient to propel a vertical axis wind turbine. In order to prove this, it must also be shown that the drag of pliable blades increases under certain angles of attack relative to the free stream, and decreases under all other angles of attack.

(b) To shed light on previously unobserved interactions between fluids and pliable structures. This specifically refers to advancing our understanding of the large-amplitude flapping instability identified during the initial wind turbine experiments.

(c) To build a full scale model of the flexible-blade wind turbine and show improved durability and maintenance characteristics in comparison to the sophisticated Windspire^{TM} vertical axis wind turbines.

1.3 Scope of Study

There is an abundance of rotor designs (see Hau (2006)) created by numerous different people. However, the goal of this thesis is not to delve into every type of turbine rotor ever brainstormed, thus the scope must be limited. The primary goal of this thesis is to present the simplest of wind turbine designs and to demonstrate the viability of using pliable materials in an engineering project. Thus, the aim of this thesis is not to optimize such a design, but solely to prove its utility.

1.4 Thesis Outline

Chapter 1 This chapter describes prior studies and explains both the scientific as well as engineering motivation behind the current study.

Chapter 2 This chapter describes the experimental set-up and methods used throughout the thesis.

Chapter 3 This chapter focuses specifically on the pliable plate response to forces generated by a surrounding fluid flow.

Chapter 4 This chapter is dedicated to the study of the vertical axis wind turbine model within the wind tunnel environment.

Chapter 5 This chapter investigates the vertical axis wind turbine model at full scale at the Caltech Field Laboratory for Optimized Wind Energy.

Chapter 6 This chapter summarizes the research contributed through this thesis and recommends further avenues of investigation for future research.

Chapter 2

Materials and Methods

First, the material properties of the blades used in the different experimental studies are discussed. Next, the wind tunnel facilities used are presented and the measurement equipment and data processing which the wind tunnel experiments have in common are explained. Finally, the Caltech Field Laboratory for Optimized Wind Energy facility is described. Further details on the set-up of the individual experimental configurations are provided in the relevant chapters.

2.1 Material Properties

Within this thesis, three primary experiments are described, namely wind tunnel and a full scale model of a wind turbine with flexible blades, as well as the inverted flapping flag phenomena which occurs during the operation of these flexible blade rotors. These experiments are primarily related by the use of pliable cantilever plates. The spectrum of materials and geometries studied in this work are specified in tables 2.1 and 2.2.

Kornecki et al. (1976) introduced dimensionless velocity (κ) and mass ratio (μ) (see equation 2.1). These two dimensionless parameters provide guidelines for the characterization of elastic plate behavior.

$$\kappa = \frac{\rho U^2 L^3}{D} \qquad \mu = \frac{\rho_f L}{\rho_s h} \tag{2.1}$$

Table 2.1. Plate Material Properties

Material	Young's Modulus (E)	Poisson's Ratio (ν)	Thickness (h)
Aluminum	69 GPa	0.33	3.175 mm (1/8 inch)
Delrin	2.4 GPa	0.35	1.5875 mm (1/16 inch)
Delrin	2.4 GPa	0.35	0.79375 mm (1/32 inch)
Rubber	2 MPa	0.49	3.175 mm (1/8 inch)
Polycarbonate	2.38 GPa	0.38	0.8 mm
301 Stainless Steel	193 GPa	0.24	0.254 mm

Where D is defined as the flexural rigidity:

$$D = \frac{Eh^3}{12(1-\nu^2)} \tag{2.2}$$

Young's modulus (E), poisson's ratio (ν), as well as plate density (ρ_s) were provided by the material manufacturer's material or matweb.com. The length (L), thickness (h), and height (H) of each plate were measured values.

Table 2.2. Dimensions of all blades and plates separated by experiment. Range of wind speed (U) and dimensionless velocity (κ) for each plate are also given.

	Material	D [Nm]	L [cm]	H [cm]	U [m/s]	κ
Turbine	Aluminum	206	25.4	40.6	2.5 - 8.5	0.00057 - 0.0066
	Delrin	0.9	25.4	40.6	2.5 - 8.5	0.13 - 1.51
	Delrin	0.1	25.4	40.6	2.5 - 8.5	1.17 - 13.5
	Rubber	0.007	25.4	40.6	2.5 - 8.5	16.7 - 193.5
FLOWE	Delrin	0.1	22.9	88.9	0.988 - 15.13	0.14 - 32.8
	Rubber	0.007	22.9	88.9	0.083 -17.75	0.014 - 645
	Stainless Steel 301	0.28	22.9	81.3	0.266 - 13.03	0.003 - 10.2
Plates	Polycarbonate	0.1	30	2.54 - 63.5	1.5 - 8.5	0.73 - 23.4
	Polycarbonate	0.1	25.5	62.2	1.5 - 8.5	0.44 - 14.4

2.2 Lab Facilities

2.2.1 Wind Tunnel

All wind tunnel experiments were performed in a wind tunnel where the flow is powered by an array of computer fans. A picture of the tunnel, which is similar in design to Johnson and Jacob (2009), was built by YuYang Fan and Daegyoum Kim is shown in Figure 2.1. The cross section of the wind tunnel is 1.2 m by 1.2, with flow speeds between 1.5 m/s - 8.5 m/s. The wind velocity was controlled through an

Figure 2.1. Wind tunnel Facility

Arduino board. Daegyoum and YuYang performed a calibration between an internal value of duty cycle (DC) to standard wind velocity units. This calibration curve was used to control the wind tunnel velocity within the tunnel. A copy of the calibration curve is provided in table 2.3.

Table 2.3. Calibration of CPU wind tunnel speed settings

DC	28.4	34.5	40.6	46.6	52.7	58.8	64.8	70.9	77	83	89.1	95.2	100
ms^{-1}	2.5	3.0	3.5	4.0	4.5	5.0	5.5	6.0	6.5	7.0	7.5	8.0	8.5

One characteristic of the tunnel is that when a particular speed is selected, the fans ramp up, overshoot the designated speed, and then ramp down to the selected

speed. Therefore, the tunnel was allowed to stabilize for at least a minute prior to recording any data.

2.2.2 Image Capture and Processing

Three high speed cameras were used to capture plate and blade movements of the experiments performed in the wind tunnel. One camera was a Dantec Dynamics Nanosense MkIII and two were Imperx IPX-VGA210-L cameras. The Dantec Dynamics Nanosense MkIII camera was used for qualitative observations of the flapping blades during wind tunnel testing of the VAWT. The Imperx IPX-VGA210-L cameras were used for measuring the flapping amplitude of the plates in Chapter 4. The Imperx IPX-VGA210-L cameras had a resolution of 640X480 pixels and the measurement plane was 576X432mm, which results in a spatial accuracy of ±0.045 mm. The cameras were mounted above the tunnel in order to provide a bird's eye-view of the experiment. A sketch and a picture of the camera view are provided in Figure 2.2a and 2.2b, respectively. Images were captured at either 100 or 207 frames per second in greyscale. Through the image processing described in appendix B, the amplitude

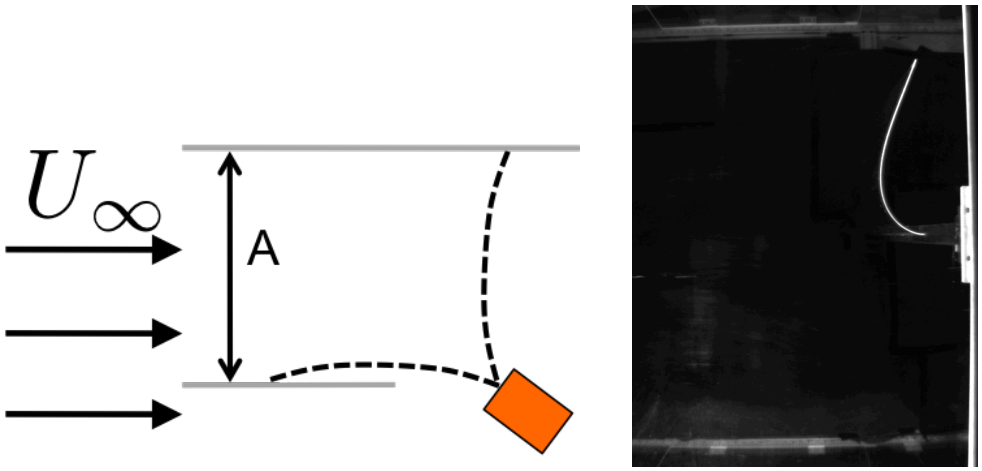

(a) Pictorial definition of amplitude (b) Example Camera Image

Figure 2.2. Birds-Eye-View of Plate behavior

of oscillation was obtained. The amplitude of oscillation was defined as the largest distance the blade tip traveled perpendicular to the direction of the free stream flow,

as shown in Figure 2.2a.

In the case of the wind turbine experiments, LabVIEW was used to trigger the image acquisition, such that torque and angular velocity data could be properly synchronized to the images. In the case of the cantilever plate experiments, reference images were captured before and after each data set. These calibration images were used to find the initial unperturbed state of the plate. Images were analyzed using Matlab's image processing toolbox. An example code for blade tip tracking is provided in Appendix B.

Due to the large number of datasets collected, it was necessary to computerize the image processing. The first step in the procedure was to modify the field of view by cropping the image to exclude superfluous information. The cropping box was manually adjusted each time the camera was moved or the plate was changed. In order to easily track the edge of the plate, images were converted from greyscale to black and white using an appropriate threshold. The threshold varied depending on the contrast achieved in the original image. Next, the Matlab edge finder tool "bwboundaries" was utilized to track the plate location. Then the base of the plate against the clamp was found. The tip of the plate, which was defined as the furthest point from the base of the plate, as calculated using the pythagorean theorem, was determined next. An array of the tip position was constructed for every test. After obtaining the maximum amplitude from the array of tip positions, the ratio of stroke amplitude to plate length was calculated. The length of the plate was established by using the reference image to translate dimensional length into pixel length.

2.3 Field Laboratory for Optimized Wind Energy

The Caltech Field Laboratory for Optimized Wind Energy (FLOWE) is located in Antelope Valley in California, USA. Winds in this region are caused by air heating up and rising over the desert to the east, which in turn causes a low-pressure region that is subsequently filled by cooler air blowing into the region from the ocean to the west (Hau (2006)). This results in a daily cycle of winds, with the highest velocities

occurring in the afternoon hours, and lulls between midnight and midday. In addition, wind velocities are higher during the summer months due to the higher desert temperatures. The winter months are characterized by a decrease in wind activities in the region.

Figures 2.3 and 2.4 show the wind conditions at the Caltech FLOWE for 2013. Figure 2.3 shows a wind rose, which displays the prevalent wind direction at the field site, along with the accompanying wind speeds. This shows that the prevailing wind direction is from the southwest. However, wind events associated with the so called

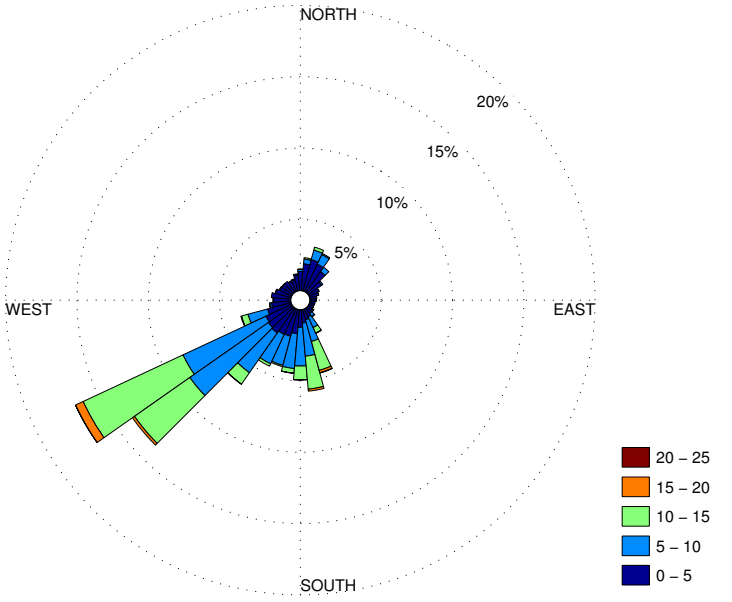

Figure 2.3. Wind rose indicating wind direction and speed at the Caltech Field Laboratory for Optimized Wind Energy for 2013.

Santa Ana winds usually occur in the fall from the northeast.

Figure 2.4 displays the wind speed, measured at 1Hz and averaged over 10 minute intervals, as is conventional in meteorology. The large spread in wind speeds reflects the diurnal wind cycle. The wind sensor was out of order for 19 days in the month

of February, leaving a gap in the data shown in Figure 2.4. The diurnal wind cycle is

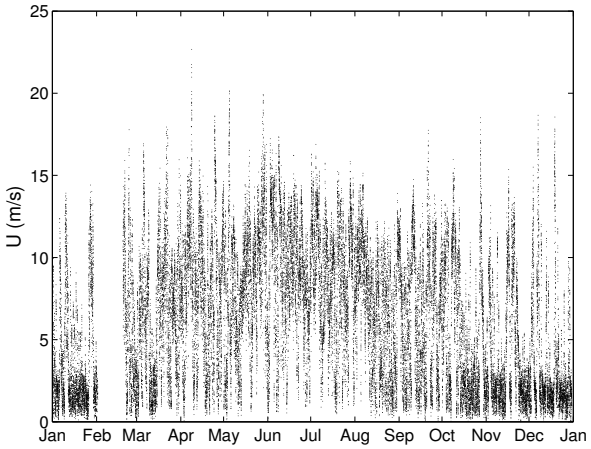

Figure 2.4. Ten minute averages of wind speed at the Caltech Field Laboratory for Optimized Wind Energy for 2013.

shown by taking ensemble-averages over 24 hour periods of time. Figure 2.5 displays wind velocities ensemble averaged over each day for the months of January and June 2013. Qualitatively the curves look very similar, with the highest wind velocities

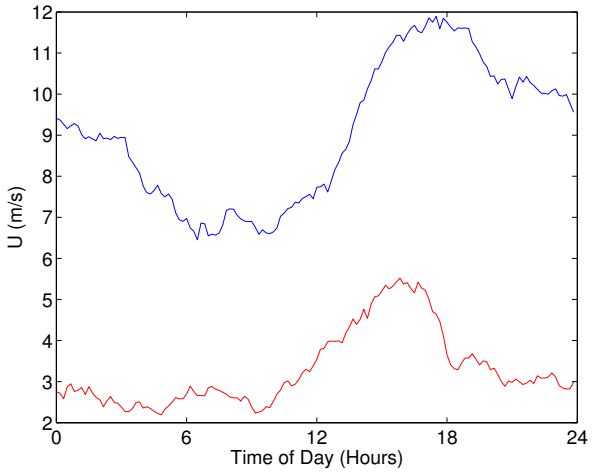

Figure 2.5. Daily average of windspeed for January (—), and June (—)

occurring in the late afternoon and gradually dying down after the sun sets. The winds then remain relatively calm until midday, when the sun has had a chance to

warm up the air above the desert floor. This agrees with the wind patterns previously described. The relatively low velocities in January reflect the decreased wind activity during the winter months, as compared with the higher velocities observed in June.

Chapter 3

Vertical Axis Wind Turbine: Wind Tunnel Testing

The work presented in this thesis stemmed from the initial goal of creating a simple and durable vertical axis wind turbine design. The wind turbine experiments conducted in the wind tunnel are described in this Chapter. The first major objective of this study was to prove the hypothesis that blade reconfiguration would produce the force differential across a turbine with otherwise symmetric blades. Such a force differential is required in order to produce power. The second objective was to provide an experiment that tests the concept of passively deforming blades.

3.1 Introduction

The initial experiments examined the performance of the wind turbine when blades with different material properties were used. These blades were rectangular plates made from materials ranging from very stiff to very pliable (see table 2.2). The results of these experiments were dramatic: the wind turbine would not sustain rotation when the stiffest blades were installed. In contrast, when each set of the pliable blades were used, the turbine rotated. Astonishingly, the blade motion between the three pliable materials was completely different from one to another, prompting further investigation.

The first set of experiments (referred to hereafter as dynamic tests) described in this Chapter were designed to test the power production by the turbine and to

compare the results between the different types of blades. Due to the influence of blade material on the dynamics and therefore on the turbine performance, images of the turbine are presented alongside the quantitative data. The second set of experiments (referred to hereafter as static tests) described in this Chapter analyzed the torque differential produced by the different blades. It was designed to explain in detail how the torque production is connected to the blade deformation and why some blade materials caused the turbine to spin while other materials prevented the turbine from spinning. Solutions from an analytical model were compared to the experimental results from the static tests where appropriate.

3.2 Materials and Methods

A generic two bladed vertical axis wind turbine was built, as shown in Figures 3.1 and 3.2. Figure 3.1 shows a side view of the turbine while Figure 3.2 shows a bird's eye-view. The left images show schematics of the turbine, while the right images show pictures of the actual set up. The turbine consisted of a vertical axis, held in place between two bearings at the top and bottom of the wind tunnel. The struts that held the blades were located on opposite sides of the turbine axis, i.e. 180 degrees apart. The blades consisted of flat, flexible plates that are clamped between two optical anglers, allowing for sensitive adjustment of the blade pitch angle, α. For dimensions of specific components, see table 3.1.

Table 3.1. VAWT dimensions

Part	Diameter	Height	Thickness	Length
Vertical Axis	1 inch	47 inches		
Turbine Arms		0.5 inch	0.5 inch	9 inches
Turbine Blades		16 inches	see table 2.1	10 inches
Blade Clamps		16 inches	0.5 inch	1 inch

Below the wind tunnel, the turbine axis attached to a Futek TRS605 20Nm torque meter and encoder, which was wired to a LabVIEW data acquisition system using

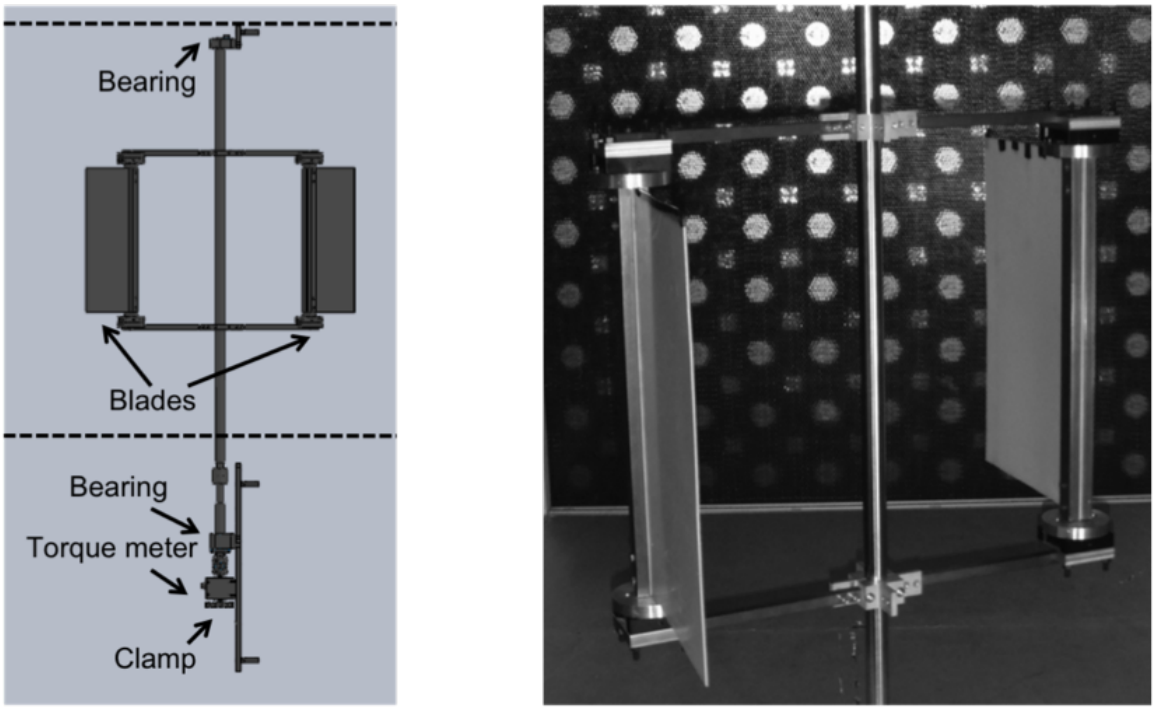

Figure 3.1. (a) Schematic of the relevant turbine parameters. Dashed horizontal lines represent the tunnel ceiling and floor. (b) Picture of the turbine in the wind tunnel. Background shows the array of computer fans that drive the tunnel.

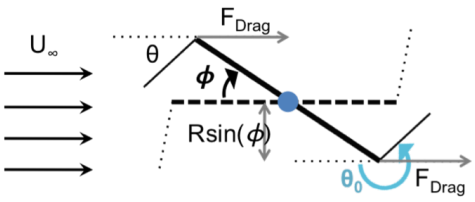

(a) schematic

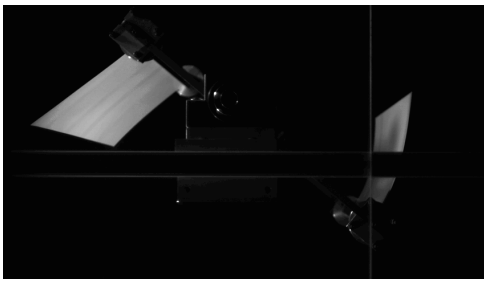

(b) picture

Figure 3.2. View from above the turbine. α is the angle of the blades relative to the tangent of the arms. ϕ is the angle of the turbine's rotation. θ is defined as the angle of attack of the blades to the free stream.

a NI PCIe-6321 DAQ card. The torque measurement had an uncertainty of ±0.1 Nm, and the encoder had an uncertainty of ±0.25°. The timing accuracy of the NI PCIe-6321 was 550pm of the sampling rate, providing an uncertainty of ±0.00000075 s. Due to the unsteady nature of the torque and angular velocity measurements, the uncertainty in power is time dependent. The maximum uncertainty in power recorded was ±0.3 Watts. On the bottom side of the torque meter, a motor was attached for the dynamic experiments. A clamp replaced the motor when the static experiments were conducted. Aluminum, acetal (Delrin), and rubber blades were tested (see table 2.2). Wind tunnel testing was conducted in the lab facility described in Chapter 2.2.1. Images of each experiment were obtained through the image acquisition system set up above the tunnel, as described in Chapter 2.2.2.

3.2.1 Wind Turbine Data Processing

Wind turbine performance is measured by the power coefficient (C_P), defined as the ratio between the power output by the VAWT to the power of the wind passing through the swept area of the blades (A_{swept}). The power coefficient, as defined in equation 3.1, was calculated and compared for each test.

$$C_P = \frac{\tau\dot{\phi}}{\frac{1}{2}\rho_{air}A_{swept}U_\infty^3} \tag{3.1}$$

where τ is the torque, $\dot{\phi}$ is the angular velocity, ρ_{air} is the density of air, A_{swept} is the swept area of the turbine as depicted in Figure 3.3, and U_∞ is the free stream velocity. The power coefficient is typically displayed as a function of tip speed ratio (λ). Tip speed ratio is defined as the ratio between the blade tip velocity and free stream velocity, as described in equation 3.2.

$$\lambda = \frac{R\dot{\phi}}{U_\infty} \tag{3.2}$$

Tip speed ratios above 1 indicate the turbine is driven through lift as opposed to drag. Therefore, tip speed ratios vary considerably depending on the turbine type

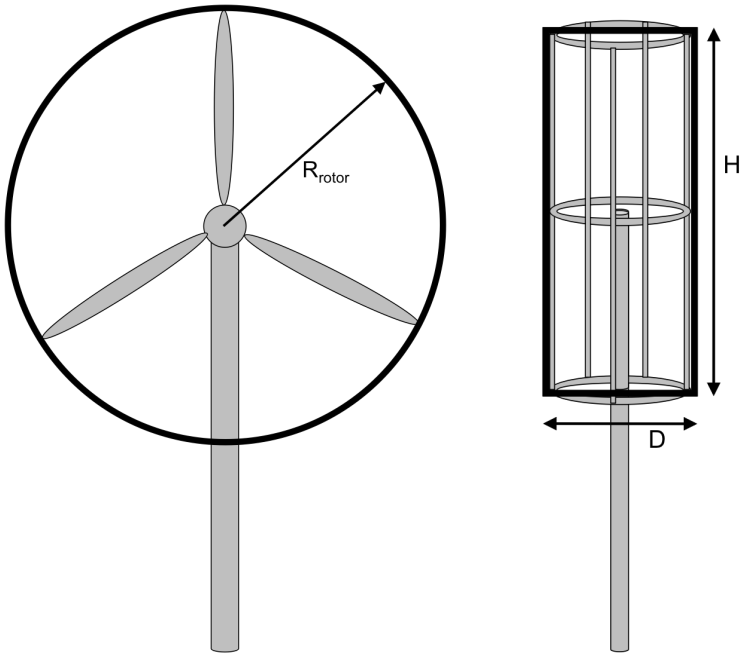

(a) $A_{HAWT} = 2\pi R_{rotor}$ (b) $A_{VAWT} = DH$

Figure 3.3. Swept area of wind turbine rotors for a (a) HAWT and a (b) VAWT.

(Hau (2006)).

3.2.2 Dynamic Tests

Dynamic testing refers to experiments run while the turbine was free to rotate. Two DC brushless motors from Anaheim Automation (BDPG-38-86-12V-3000-R14, BDPG-40-12V-5000-R27) were used to provide a back torque against the turbine rotation. The power input into the motor was raised by small increments in voltage (0.2-0.3V). This adjusted the speed and torque of the motor, providing a method to mimic loading of the turbine by a generator and inverter system. The power curves for the different rotor configurations were measured by varying the motor load at a fixed wind tunnel velocity and repeating the procedure over the relevant range of wind tunnel velocities.

3.2.3 Static Tests

Static testing refers to experiments run while the turbine was clamped (unable to rotate) at 15 different angles of rotation. During these tests, torque (force differential across the turbine) was recorded while high speed images of the blade behavior were collected. This allowed for a comparison between the blade behavior and force differential across the turbine.

3.2.4 Analytical Solution

The analytical solution is based on the theoretical work described in Gosselin et al. (2010) and Luhar and Nepf (2011). The analytical solution is only applied to the cases where the blade undergoes reconfiguration, and was neglected when the blades underwent large amplitude flapping. This is because the analytical solution assumes that the flow is quasi-steady.

3.3 Results and Discussion

The dynamic test results investigating VAWT performance as a function of blade angle (α) are discussed first. Next, the unanticipated blade flapping and the effect on turbine performance are examined. In an effort to better understand blade behavior, tests done on the static turbine are presented. In the last Section, the analytical theory is compared to the experimental results.

3.3.1 Dynamic Tests

Preliminary testing investigated the effect of blade pitch angle, α, on the turbine's performance. The blades used for this test were a flexible plastic sold as Aquaflex. Figure 3.4 displays the turbine power coefficient against the angular velocity of the turbine. Blade pitch angles of 0°, 5°, 15°, 25°, and 45° were tested. The power coefficient (C_P) is maximized as blade pitch angle (α) decreases. The power coefficient

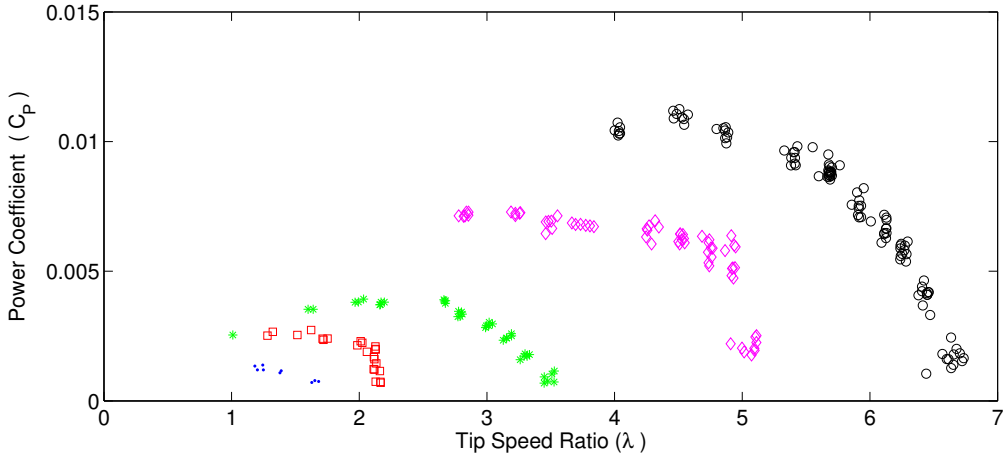

Figure 3.4. Effect of changing the blade pitch angle (α). Plots show C_P vs. λ for 45°○, 25° □, 15° *, 5° ◇, and 0° ○

plateaus over a range of tip speed ratio when $\alpha = 5°$. All future testing performed at $\alpha = 5°$.

Next, dynamic tests were conducted with all four different blade materials. Of the aluminum, plastics, and rubber blades tested, all enabled the turbine to rotate except for the aluminum blades. As a consequence, power curves could not be obtained for the turbine when aluminum blades were attached. Therefore, the following Section presents results for the turbine tests performed when the three sets of pliable blades were attached.

The first discovery was that the rotor propelled itself as a result of violently flapping blades. Figure 3.5 shows a sequence of images taken by the high speed camera and the corresponding curves for the power output during a large amplitude flapping event. In all images the free stream flow moves from left to right, and the turbine rotates clockwise. The blades in the example are 0.8 mm thick Delrin plates. The free stream velocity was 6.5 m/s, and the motor provided a load of 0.45 - 0.75 Watts. This load is large enough that the turbine is close to being incapable of rotation. As the turbine approaches standstill, because of the large load, the turbine approached the static limit discussed in depth in Section 3.3.2.

Images **A-H** are looking down at the turbine, and show the blade motion at the

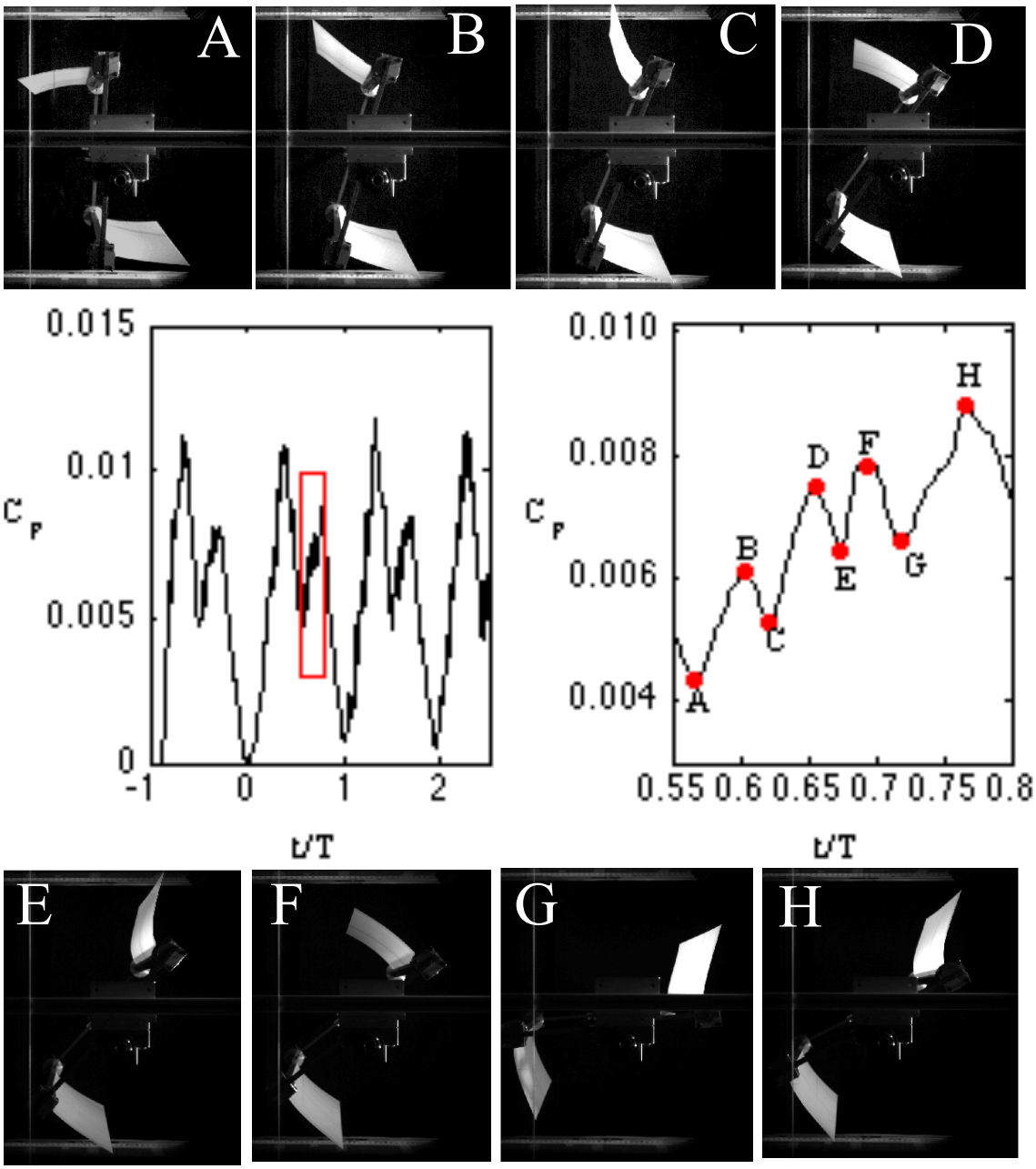

Figure 3.5. Images A-H correspond to the points labeled on the power plot. Air flow moves left to right and the turbine is rotating clockwise around its vertical axis.

corresponding points in the power data. The top blade in the picture is moving with the wind and will be referred to as the downwind blade, while the blade in the bottom of the picture is moving against the wind and will be referred to as the upwind blade. The downwind blade is on the side of the turbine that is producing positive torque in Figure 1.1. Likewise the upwind blade produces negative torque. The plot in the center left shows the power curve over 3.5 rotor revolutions and the plot in the center right magnifies the region where images **A-H** occurred.

Point-**A** corresponds to the point of lowest power production, which occurs every half rotation. This occurs just before the downwind blade catches the wind, resulting in the turbine picking up speed and increasing the power production. Between points-**B** and **C** the downwind blade is bending away from the wind in a process known as reconfiguration. This leads to a decrease in power output from the turbine. At point-**C** the blade reverses direction in its flapping, i.e. moves against the free stream direction. This increases the relative velocity seen by the blade and enhances the power output to the level at point-**D**. The cycle repeats itself two more times between points-**D** and **E** and once again between points-**F** and **G**. Point-**H** corresponds to the point where the upwind and downwind blades switch, with the previously upwind blade becoming the downwind blade and thus the power producing blade.

It is notable that large-amplitude flapping only occurs when the turbine has a substantial load applied to it. This flapping behavior is further investigated in Chapter 4, where it was found that the relative velocity of the blade is most important in predicting blade behavior. The relative velocity is defined in equation 3.3

$$V_{REL} = U_\infty - R\dot{\phi}\sin(\phi) \tag{3.3}$$

Figure 3.6 shows the relative velocity between the free stream and the velocity component of the blade that is parallel to the free stream for two distinct tests with different loading conditions. From Figure 3.6 it can be seen that the relative velocity falls between 7-10 m/s for the low load case and between 6 - 6.9 m/s for the high load case. Close examination of the velocity curve for the high load case reveals oscillations

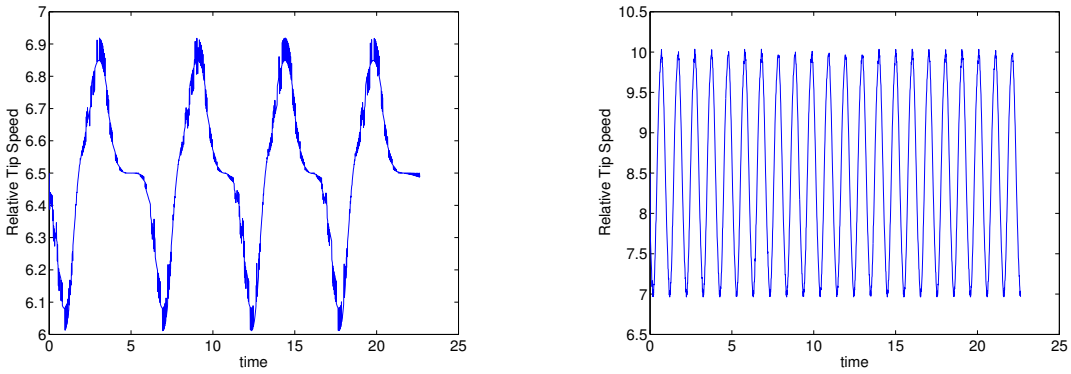

(a) High Load (b) Low Load

Figure 3.6. Relative velocity of single blade over time.

that correspond to the flapping behavior of the blade. These oscillations are absent in data from the low load case.

Using the dimensionless velocity, κ is calculated through equation 2.1 using the relative velocities 6 m/s, 7m/s, and 10 m/s. This yields κ values of 6.75, 9.2, and 18.75, respectively. As will be discussed in Chapter 4, flapping is shown to occur roughly between $2.7 < \kappa < 9$. By examining Figure 3.6 we see that when a sufficient load is applied to the turbine, the relative velocity is within the range where flapping is expected. However, at lower loads, the relative velocity is too high for large-amplitude flapping to occur. This finding matches qualitative observations of the blade behavior for each of these cases.

Figure 3.5 center shows how the power generation varies over the course of one rotation as the blades move in and out of the regions where they produce torque. It also shows how the power varies due to the flapping motion in a high load case. However, it can also be seen that the power production isn't equal between the two identical turbine blades. For a deeper analysis, Figure 3.7 displays the power data for one period of rotation (T) after it has been passed through a low pass filter to more obviously show this pattern. Figure 3.7a shows data from a turbine which is loaded via the motor, whereas Figure 3.7b shows data where the turbine has no additional load applied to it. While the blades set-up on either side of the turbine are

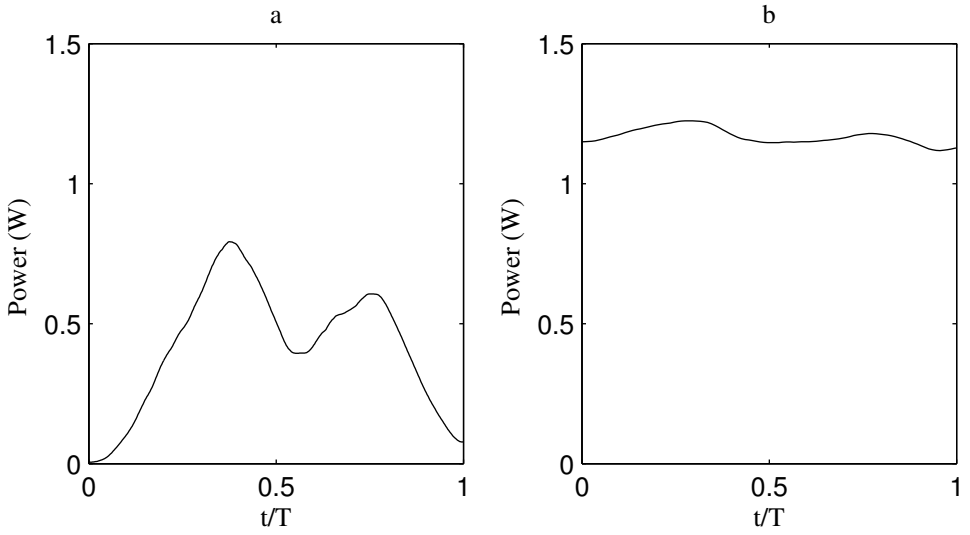

Figure 3.7. Low pass filtered power data over the course of one full rotation for the turbine (a) with a load applied and (b) unloaded.

built to be identical, the power output is not. This likely stems from several factors, including small geometric differences between the two blades. While the imbalance between the torque production between blades is obviously amplified through loading, the trend still exists even when the turbine is unloaded. Figure 3.7 shows that the imbalance in the power production between the two blades decreases with the load and therefore with the intensity of the flapping events that occur. The imbalance is observed by the occurrence of two non-symmetric peaks in power output for each period of rotation. Since the asymmetry occurs under all loading conditions, it is likely that this phenomena is caused by the nature of the flapping event.

To investigate this further, Figure 3.8 shows the relative velocity of both blades of the turbine over four rotations. It is clear that one blade (shown in red) experiences a higher relative velocity than the other blade (shown in blue) on both the downwind and upwind part of the rotation. The relative velocity is a direct result of the blade dynamics, and small differences can have a substantial impact on the behavior of the whole turbine, including the power output. The curves in Figure 3.8 intersect twice over each rotation, however, the curves feature a saddle point only every other intersection. The intersection at the saddle points of the two curves indicates a

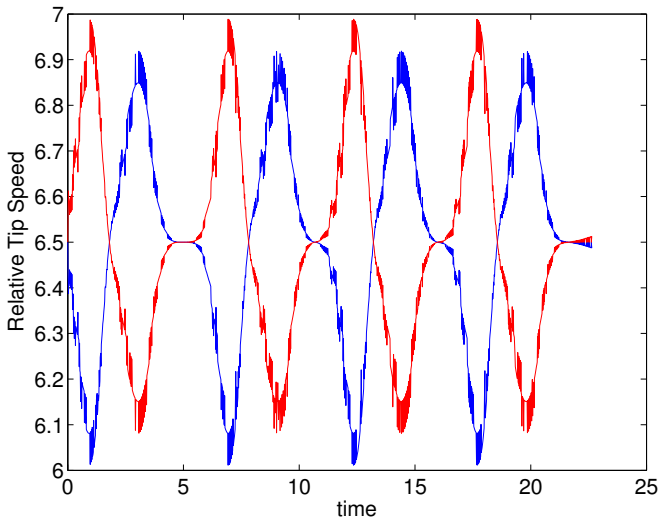

Figure 3.8. Relative velocity of both blades of the turbine over four rotations. The red curve (—) corresponds to the blade experiencing higher relative velocities than the blade represented by the blue curve (—).

position where the turbine briefly stops, and the blades experience the same relative velocity. As shown in Figure 3.5, a high enough load can cause the turbine to cease rotation before a flapping event kick-starts rotation again.

A flow diagram that illustrates how the flapping blades may cause such a variation in behavior is shown in Figure 3.9. When the turbine moves against a strong resistance, its rotational speed decreases and the relative velocity of the blades increases during one half of the cycle. If the relative velocity falls into the right range a large flapping event occurs, giving the turbine a significant power boost. This power boost increases the rotational speed of the rotor to the point where the next blade experiences a lower relative velocity and experiences a small flapping event when it passes the appropriate position. The power produced by the small flapping event isn't sufficient to maintain the rotational velocity of the turbine, and by the time the first blade returns to the position where flapping occurs, the relative velocity is high enough again to cause a large flapping event.

The magnitude of the changes in the relative velocity, as seen by the blades, over the course of several turbine rotations is shown in Figure 3.6. The discussion related

to the diagram in Figure 3.9 explains why large amplitude flapping does not occur for all loading cases but only when the load is sufficient to place the turbine in a flow regime close to its stall point (compare Figure 3.6 a and b).

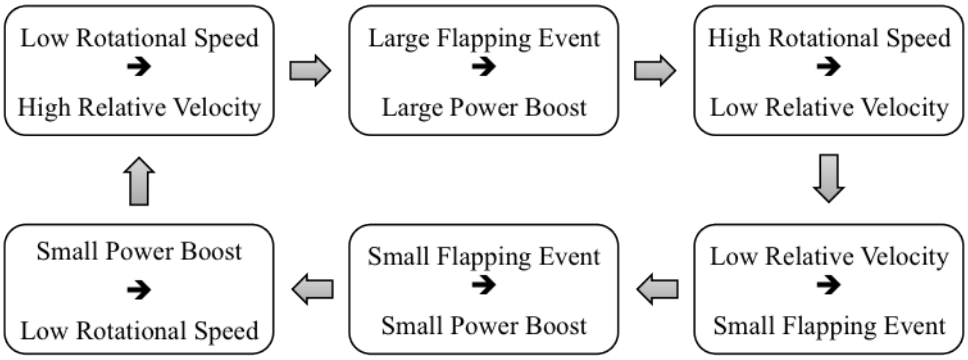

Figure 3.9. Cycle of high power output to low power output during one turbine rotation.

Figure 3.10a shows the span of power coefficients over angular velocity that occurs over the course of a rotation for different tip speed ratios. Figure 3.10b displays the power curve that is derived by averaging the data from Figure 3.10a over a single rotation. The instantaneous power curve (Figure 3.10a) is a result of the unsteady angular velocity throughout one rotation. Both curves are for the turbine when the $\frac{1}{32}$ inch thick Delrin blades were installed. Unlike other turbines, where the power curve cuts off well before the turbine reaches a zero angular velocity, it is noted that this particular turbine's power curve stretches into negative angular velocity. When a sufficiently high load is applied to the turbine, the turbine will start to counterrotate briefly. Reverse motion was observed up until the point that the turbine's position allowed for blade flapping to commence. The turbine would react to the impulsive force resulting from the flapping, and start rotating forwards. This demonstrates a self-starting mechanism unlike any other VAWT. While the regime in which the turbine rotates in reverse doesn't generate power, test results indicate a solution to the standard start-up problems of typical vertical axis wind turbines. In addition, it is hypothesized that this reverse motion can be eliminated through adding additional blades, appropriately distributed, on a full sized turbine model. By adding blades,

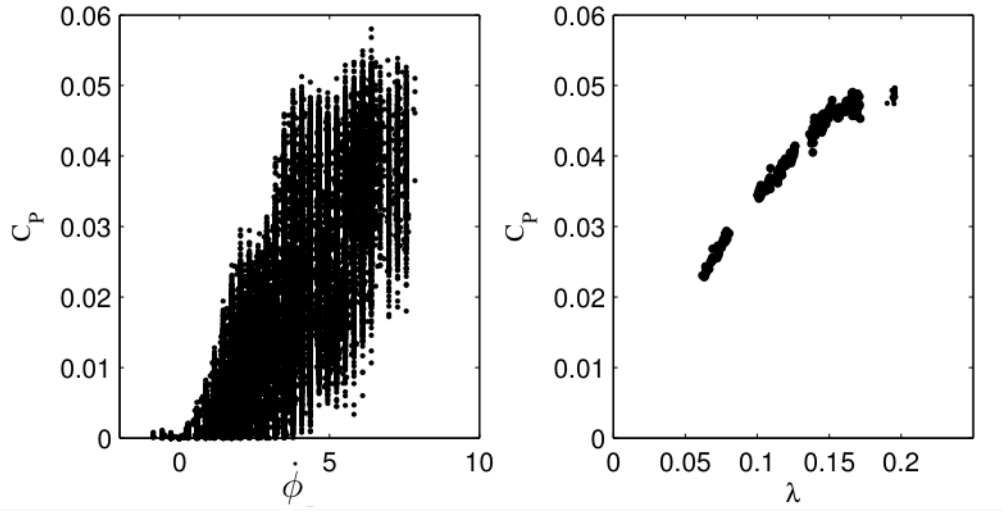

Figure 3.10. Turbine efficiency as measured by the power coefficient (C_P) over tip speed ratio (λ). (a) raw data and (b) averaged over rotation.

the turbine would receive more continuous forcing from the wind acting against the blades.

At this point it had become obvious that the blades were going through more complicated motions than simple reconfiguration. Unexpectedly, large amplitude flapping appeared to propel the turbine. Figure 3.11 breaks down the blade orientation at various stages of rotation. Shaded regions of the right turbine image are correlated with specific behaviors, and will be described in detail in Section 3.3.2. The dark grey region represents the general region where flapping blades were observed. The light grey region indicates the area where the front blade blocks the rear blade, preventing the free stream from interacting with the rear blade. Pictorial representations of the blade (a.k.a. an elastic cantilever plate) and clamp are shown to emphasize the constantly changing orientation of the blades as the turbine spins.

Follow-up studies were conducted to further understand this unforeseen flapping behavior. The first study (Chapter 3.3.2) investigated the turbine when the turbine was secured to prevent rotation. The second study (Chapter 4) investigated elastic cantilever plates in a flow oriented such that the leading edge was free to move and the trailing edge was fixed by a clamp.

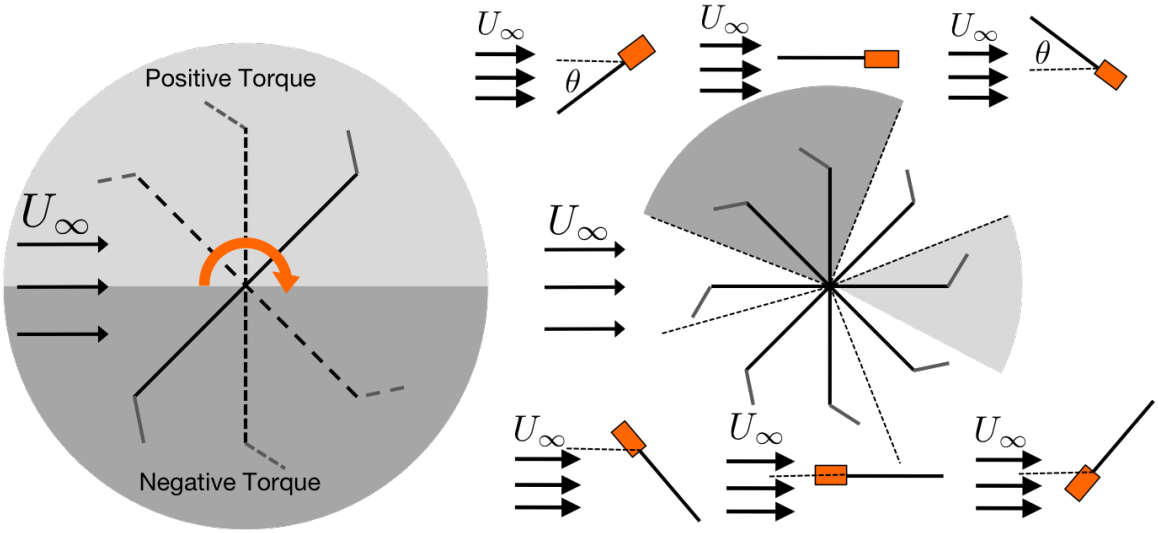

Figure 3.11. Blade orientation during various Sections of turbine movement.

3.3.2 Static Tests

Static testing was performed to compare the force differentials across the turbine obtained by different blade types. Due to geometry, the turbine would experience no force differential if the blades behaved the same on both sides of the turbine. However, force differentials did occur as a result of the differences in the blade dynamics due to their individual material properties.

The chart in Figure 3.12 shows the torque or force differential across the turbine for a set of wind velocities for the stiff, aluminum blades. The lower graphic shows the bird's eye-view of the turbine for each of the static positions tested. Unlike the other blades tested, these blades do not deform within the range of wind velocities tested. Within the range of velocities studied, higher velocities correspond to a higher torque of the turbine. Depending on the blade position, this torque can be positive or negative. While increasing wind speed increases the torque produced by the blades, the net torque integrated over a full turbine rotation is almost zero over the full range of wind speeds tested. Since the trend shows that wind velocity simply increases the magnitude of the effect, the following tests focus only on one wind speed, specifically at 8.5 ms^{-1}. Figure 3.13 shows the torque exhibited at 15 different turbine angles for

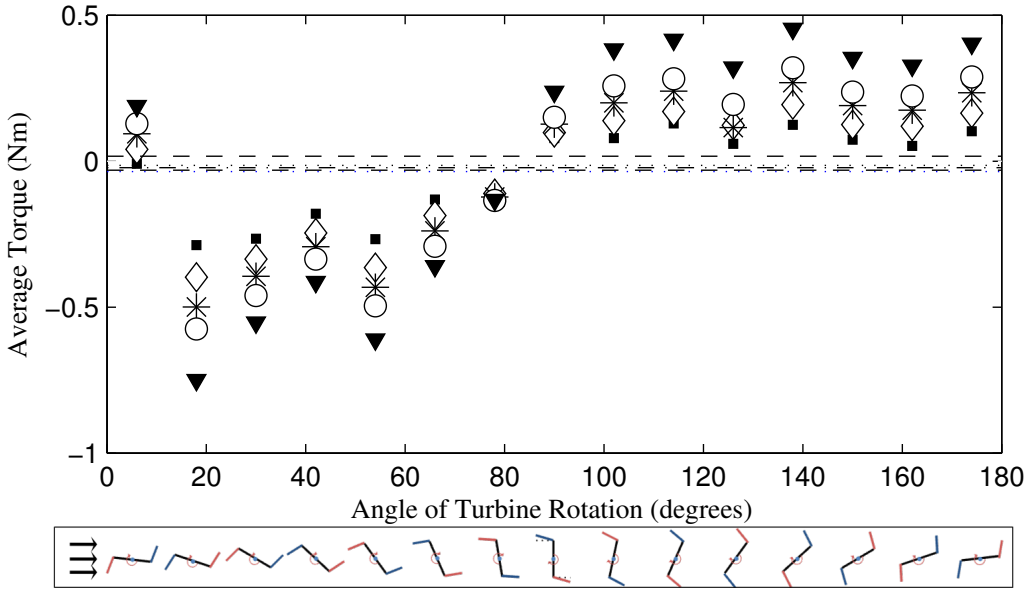

Figure 3.12. Static tests of the turbine with rigid blades ■ 5m/s ∘ 5.9 m/s ∗ 6.9 m/s ◊7.5 m/s ▼8.5 m/s. Lower box provides aerial view of the turbine's clamped position.

four different blade types.

Figure 3.13a shows the data with error bars corresponding to the standard deviation of the torque, while Figure 3.13b shows a magnified version of the same plot. The data points within the dark grey region of the Figure show very large error bars. Within this region, the delrin blades were observed to flap, which in turn exerts an unsteady force on the turbine. This results in loading and unloading the turbine and therefore a large standard deviation of the measured torque. The light grey regions show an area in which the undisturbed flow is merely acting on the forward blade, as the rear blade is located in the shadow of the forward blade. The result is a highly complex flow caused by the rear blade interacting with vortices shed from both the forward blade and vertical axis of the turbine. The result is an unsteady load on the turbine, which leads to a high standard deviation in the measured torque. The shaded regions correspond to the shaded regions in Figure 3.11. The flow in the remaining regions is dominated by the reconfiguration of the blades.

As in Figure 3.12, the average torque over the full rotation is shown with horizontal

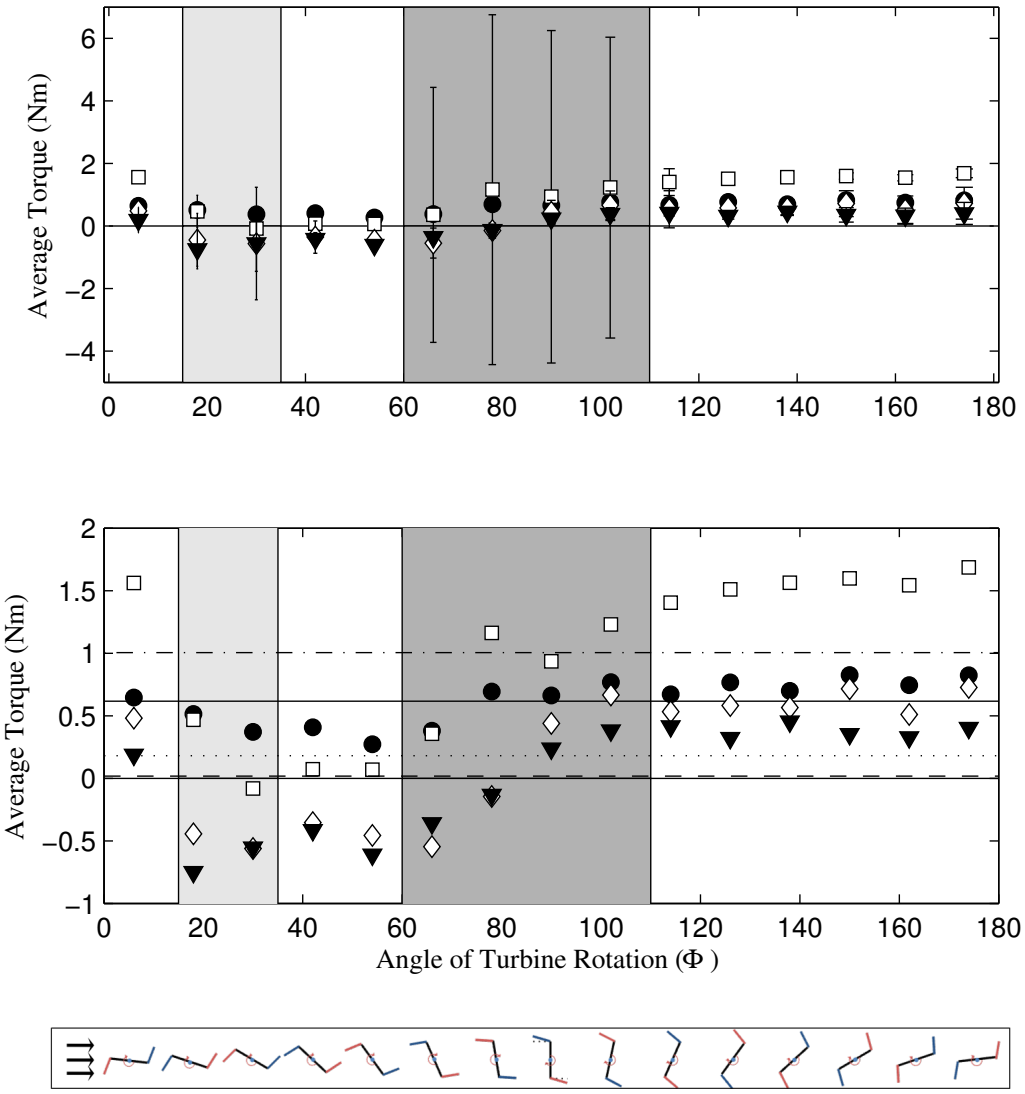

Figure 3.13. Comparison of turbines with various blades. Figure (a) displays error bars (standard deviation), whereas (b) provides a clearer view of the data. □ 1/32 inch delrin – · average of 1/32 inch thick delrin • rubber blades — average of rubber blades ◊ 1/16 inch thick delrin · · · average of 1/16 inch thick delrin ▼ rigid blades - - - average of rigid blades.

lines in Figure 3.13. Unlike the rigid aluminum blades, the average torque over one rotation is positive for the pliable blades. This demonstrates that the turbine with pliable blades has a preferential torque direction! Average torque values are provided for reference in Table 3.2.

Table 3.2. Values of torque averaged over all 15 clamped angles

Blade Type	Average Torque of Full Rotation [Nm]
Aluminum	0.02
Delrin (1/16")	0.18
Rubber	0.62
Delrin (1/32")	1.00

Figure 3.14 shows the flapping amplitude over blade length versus the angle of the rotor position for the delrin 1/32nd inch plates. The upper graph shows the blade moving downstream, i.e. producing power. The lower graph shows the blades which are moving upstream, i.e. adding resistance to power production. These charts show that blades only experience large amplitude flapping when moving downstream. This is when the blade enters the inverted orientation discussed in detail in Chapter 4. Nevertheless, the downstream data does indicate that there is a small region where flutter may be experienced by the blade. However, the motion of the large amplitude flapping propagates through the whole turbine. As a result, some of the motion visible in the downstream blade could be attributed to the fact that the whole turbine is vibrating and not necessarily indicative of flutter.

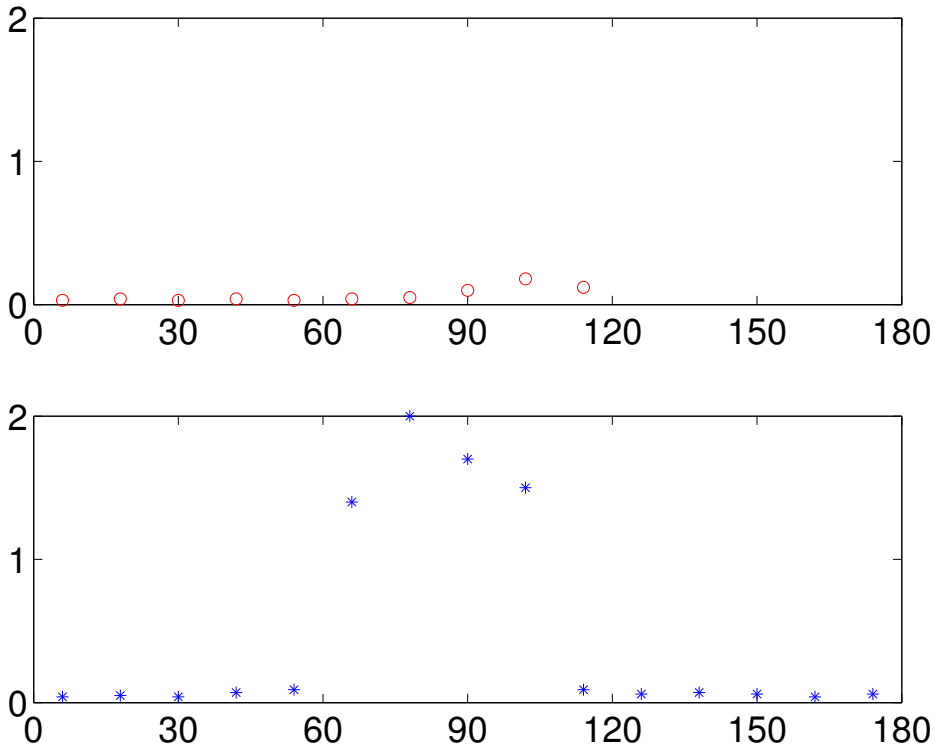

Figure 3.14. Flapping amplitude over blade length for 15 different rotor positions for (a) the upstream and (b) the downstream blade.

3.3.3 Analytical Solution

The analytical solution provides an idea about the turbine dynamics if only reconfiguration of the blades is considered. The model (see Appendix C) calculates the blade deformation based on drag but can't capture flapping behavior. Since the rubber blades most closely match a situation where only reconfiguration occurs, only this and the rigid aluminum cases were compared to their respective analytical solutions. Figure 3.15 shows the analytical solution predicted by the model compared to the static experimental results for the aluminum and rubber blades.

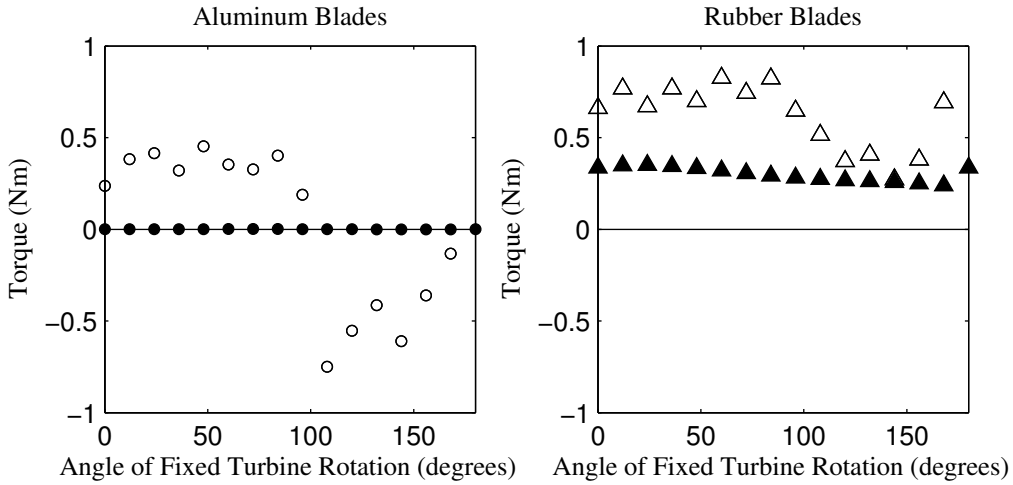

Figure 3.15. Comparison of static torque between experimental and analytical data. Filled in symbols are the results predicted from the analytical model. Hollow symbols are the experimental results.

As observed in the experiments, the model shows that the force differential across the turbine is only created when pliable blades are in use. In the case of the stiff aluminum blades, the force differential is nonexistent.

However, while the average torque values are comparable for the experimental and analytical solutions, in the case of the aluminum blades the model fails to capture appropriate torque values at different angles of turbine rotation (ϕ). As mentioned above, the analytical solution neglects lift forces acting on the blade, and focuses purely on drag. Since the model considers only the drag force acting on the blades, any torque inducing moment from the rigid blades occurs as a result of other effects,

such as lift, rather than reconfiguration. This is in contrast to the rubber blades, for which the analytical and experimental results match more closely. This indicates that the behavior of the turbine blades are largely independent of lift effects.

This model is powerful in that it also predicts the deformed shape of the reconfigured blade. Figure 3.16 shows the shapes predicted by the model, compared to snapshots of the turbine during static testing, for three different angles of turbine rotation. In all three cases, the reconfigured shape of the rubber blades matches

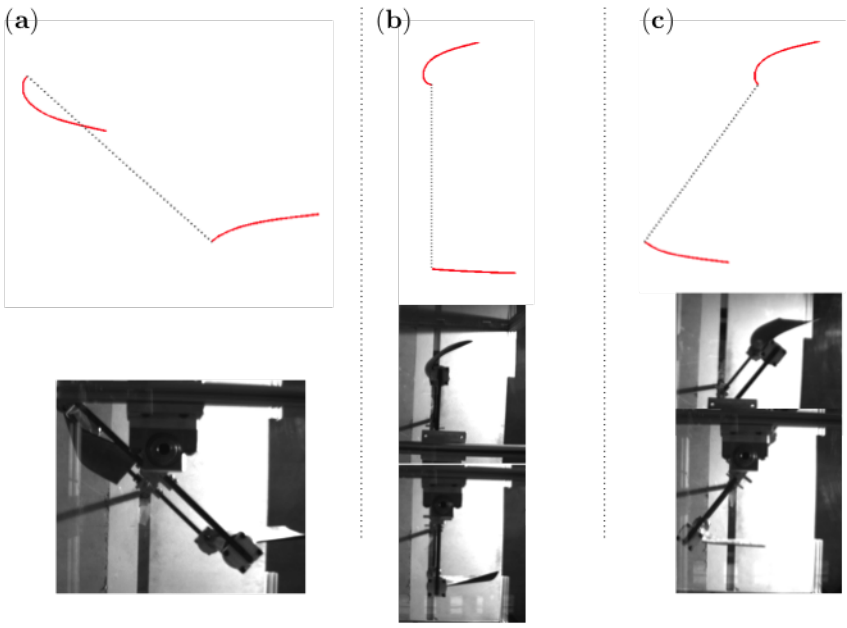

Figure 3.16. The top row shows the deformation predicted by the model for Ca=158 and the bottom row shows the images taken during static testing of the turbine with rubber blades attached. Dashed lines indicate blade arms, while red lines indicate deformed shape of turbine blades.

the expected reconfiguration from the analytical results. The only exception is the shape deformation of the blades due to gravity, which is not captured by the model. However, this deformation is small compared to the one caused by the flow and the effect is negligible. This model demonstrates that drag is sufficient to reconfigure the rubber blades and provide the necessary torque differential to achieve rotation.

3.4 Concluding Remarks

The vertical axis wind turbine was able to spin only when the pliable blades were installed. This shows that pliable blades are an incredibly simple wind turbine design that is able to produce power. Granted, the design is not as efficient as many of the current VAWTs. However, flexibility has the potential to provide damage prevention as much of the large forces during winds will simply bend the turbine blades out of the way, thus minimizing the forces exerted on the arms and the rest of the wind turbine. Such damage is explored further in Chapter 5.

Increases in wind velocity cause increased power output over the range of wind speeds tested in the wind tunnel. Within each 360° rotation, local peaks and valleys exist, corresponding to the number of blades on the turbine. Thus, by increasing the number of blades, the power output of the turbine could be steadied.

During wind tunnel testing of the VAWT design, it was found that there were different regions where the blades go through different modes of behaviors. The mode of large-amplitude flapping was unexpected and motivated a thorough study of such behaviors, covered in detail in Chapter 4.

Wind tunnel tests demonstrate the potential of the rotor. Given this favorable performance, the next step was to build a full scale model and install the turbine at the Caltech Field Laboratory for Optimized Wind Energy (FLOWE). The full scale wind turbine is discussed at length in Chapter 5.

Chapter 4

Cantilever Plates, Boundary Conditions, and Fluid Forcing

4.1 Introduction

Humans are fascinated with nature's use of pliable materials. From the wings of insects and birds, to fish and other aquatic forms of propulsion, to flags fluttering and leaves rustling, nature has a way of utilizing structures that mesmerize the human eye.

Over the last several decades, the interaction between highly pliable materials and fluid forcing has been a topic of interest in the literature. Several types of interactions have been observed between elastic cantilever beams and a fluid flow.

Flexibility typically reduces the impact of forces. Kim and Gharib (2011) showed flexibility decreases the impulsive force of a plate impulsively starting to move. Vogel (1989) and Gosselin et al. (2010) show how flexibility decreases drag. In addition, flexibility is also associated with the fluttering flag instability.

Mathematical descriptions of the movement of flexible plates can be extremely complicated. Therefore, mathematical models often aim for understanding the leading order mechanisms responsible for the plate and flow behavior. This chapter discusses the behavior of flexible plates when exposed to fluid flow. A large amplitude flapping mechanism is defined. New instability is explored and placed into the context of other studies.

4.1.1 Motivation

The wind turbine experiments discussed in chapter 3 revealed a large amplitude flapping instability, which occurred when the blades were oriented at an angle of attack roughly between $-20^\circ < \theta < 20^\circ$. Further study of this instability revealed a fluid-structure interaction problem within a range of previously unstudied boundary conditions. This chapter aims at filling in the gaps surrounding this instability.

The discovery of this new flapping instability in the context of an experimental wind turbine shows the relevance of the problem to the wind and hydrokinetic energy communities. Further examples include the investigation of fluttering flags (Akcabay and Young (2012)) as possible energy harvesting devices, such as the energy harvesting eel (Taylor et al. (2001)). Other concepts, such as the flutter-mill, have been theorized, but remain unproven experimentally (Tang et al. (2009)).

4.1.2 Literature Review

As discussed in chapter 1, elastic cantilever plates were previously studied under several contexts. Previous studies can be categorized into two main groups: the fluttering flag (Taneda (1968); Kornecki et al. (1976)) and shape reconfiguration due to drag studies (Vogel (1984, 1989); Alben et al. (2002); Gosselin et al. (2010); Luhar and Nepf (2011)). These groups can further be categorized by the boundary conditions of the elastic plates. In the investigations into the fluttering flag, the plate was aligned parallel to the flow direction and the leading edge of the plate was tethered, with the trailing edge free to move. In contrast, during the studies on drag reduction due to reconfiguration the plate was aligned perpendicular to the oncoming flow. Hence, the two different boundary conditions lead to two different plate behaviors. The investigations regarding the fluttering of flags focused on the dynamic motion of the flags due to flow instabilities. The studies on reconfiguration considered a quasi-steady condition where the hydrodynamic forces are in balance with the elastic forces of the material. It is worth noting that many of the previous studies used slender body approximations. In contrast, Kornecki et al. (1976), develops the mathematical

framework to describe 2D approximations of the plate behavior.

Notably, these two well-studied configurations are not the only configurations where an elastic plate interacts with a fluid flow. In fact, unlike the interaction between a rigid plate and fluid flow, the interaction of an elastic plate and fluid flow depends greatly on the location of the clamp or tether holding the plate in place. Thus, while the plate is parallel to the flow, the plates reaction to the flow depends on where the plate is clamped. The fluttering flag s characterized by the boundary conditions where the leading edge is clamped and the trailing edge it left free. Inverting the boundary conditions by leaving the leading edge free and clamping the trailing edge reveals the plate undergoing yet another type of dynamic behavior (see Kim et al. (2013)). These examples highlight the variation of elastic behavior, which is dependent on both the angle of attack of the plate with respect to the free-stream flow as well as the position and means of fixing the elastic plate.

In fact, only three experiments examine similarly inverted configurations, i.e. Etnier and Vogel (2000); P. Buchak and Reis (2010); Rinaldi and Paidoussis (2012). The first study, Etnier and Vogel (2000), is an investigation into drag reconfiguration of a daffodil. The daffodil was held by its stem and the drag coefficient was found over a range of velocities when the flower was held in both the conventional (fixed leading edge, free trailing edge) and inverted (free leading edge, fixed trailing edge) configurations. When tested in the inverted configuration, it was observed that the daffodil flower twisted away from the wind. Thus, the stem's stiffness was low enough to allow rotation, hindering any possibility for the flower to enter the large amplitude flapping state. As the reconfiguration progressed with increasing wind velocity, the flower head eventually twisted around completely, pointing downstream in a conventional configuration. In addition to twisting, the drag coefficient was found to decrease with increasing velocity due to the reconfiguration.

The second study, P. Buchak and Reis (2010), involved a stack of thin and low aspect ratio pieces of paper which were clamped by their trailing edge and pointed upstream. They observed a periodic opening and shutting of the papers when under the influence of wind. Strikingly, there appears to be two reasons that the clapping

book does not fall under the large-amplitude flapping as described in this chapter. As will be discussed, a large enough aspect ratio must be present prior to large amplitude flapping. The slips of paper had an aspect ratio of 0.16, which is below the aspect ratio necessary for flapping to occur. These experiments were conducted between $8.8 < \kappa < 220$, which would indicate, based on the present experiments and theory which neglect gravity, that the sheet would be in a bent-back state. In this set of experiments, one page initially enters a bent-back state. A second page bends back and joins the first, effectively increasing the thickness, which in turn modifies the stiffness of the merged sheets. The theory developed in this chapter shows that this increased thickness actually causes the merged sheets to reduce κ, decreasing the extent of deformation. As pages continue to accumulate, the deformation decreases to the point where the tip angle reduces to less than 90° (perpendicular to the flow) and the pages collapse due to the pull of gravity, returning to the initial closed-book configuration.

The final study, Rinaldi and Paidoussis (2012), examined the dynamics of a cylinder held at the trailing edge with the free edge pointing into the wind. In addition, the study examined the effects of changing the shape of the leading tip of the cylinder. While this study observed minor oscillations, large amplitude flapping as described in this chapter wasn't present. As with the P. Buchak and Reis (2010) study, the aspect ratio of the cylinder was below the range where large amplitude flapping would occur.

Our initial tests investigated the effect of mass ratio and defined three regions of behavior (Kim et al. (2013)). The first region is a straight mode, characterized by the plate fluttering slightly yet ultimately remaining in the initial configuration. This first mode occurs at low wind speeds. By increasing flow velocity, the plate enters the second state of large amplitude flapping. As velocity is increased still further, the plate enters the bent-back mode where the plate stops flapping and bends backwards away from the flow. This state is referred to as reconfiguration. Kim et al. (2013) also measured drag coefficient, finding that maximum drag was achieved during large-amplitude flapping. Furthermore, particle image velocimetry (PIV) was performed during flapping, and vortex shedding was observed to occur

each time the plate reached maximum deflection and reversed direction.

The following chapter discusses several sets of experiments investigating the boundaries of the region where large-amplitude flapping occurs. The initial results of the experimental work presented in this thesis were This work follows the previous study, Kim et al. (2013), expanding on the effect of aspect ratio and angle of attack to better understand the blade behavior observed in chapter 3. Through the experiments discussed in the following chapter, insight into the underlying physics is obtained.

4.2 Materials and Methods

A single elastic plate was held in the wind tunnel by its trailing edge, leaving its leading edge free. The plate stiffness was high enough that the plate stood revet against the force of gravity, but low enough that hydrodynamic forces were able to deform the plate. In every experiment, the plate was clamped firmly between two aluminum rods. The angle of attack (θ) is defined as the angle between the centerline of the blade and the free stream, as shown in figure 4.1.

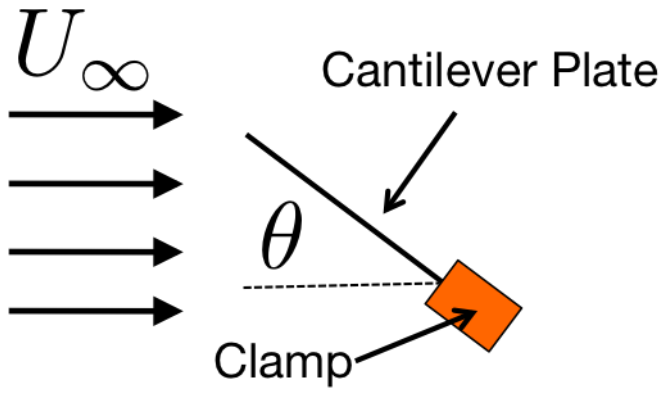

Figure 4.1. Birds-eye-view of the cantilever plate. θ is the angle of attack of the plate with respect to the free stream. $\theta = 0°$ describes the inverted flag, while $\theta = 180°$ describes the conventional flag geometry.

Length (L) is defined as the length of plate protruding from the clamp. Plate height (H) and thickness (h) were recorded for each plate tested. Plates were subjected to a range of wind velocities between 2.5 m/s $< U_\infty <$ 8.5 m/s. Plate trajectory

was recorded through a high speed camera installed above the tunnel. Images from the high speed camera were analyzed to find blade position as a function of time (see Appendix B). Then the amplitude of flapping was determined, specifying the regime of behavior for each particular configuration.

4.2.1 Theoretical Development

Experimental work on the flapping behavior of an elastic cantilever beam was performed in conjunction with John Sader's theoretical contributions. Full understanding of the flapping mechanism requires the presentation of both experimental work and theory simultaneously.

The theoretical approach was broken into two parts: the first part explains the mechanism leading to flapping, and the second part describes when the plate stops flapping and enters a reconfigured state. In Kornecki et al. (1976), the forward problem of the fluttering flag, where the leading edge of the plate is fixed and the trailing edge is free, is explored through a linear stability analysis. Kornecki et al. (1976) starts with the governing equation (4.1) below

$$0 \quad = \quad D\frac{\partial^4 w}{\partial x^4} + \rho_s h L^4 \frac{\partial^2 w}{\partial t^2} + L^4 \Delta p \tag{4.1}$$

where D is the flexural rigidity, w is the deflection of the plate, x is the axis parallel to fluid flow, ρ_s is the plate density, h is the plate thickness and L is the chord length of the plate. The plate is initially assumed to be infinite in height (H). Δp is the aerodynamic pressure acting on the plate, ρ is the fluid density, U is the fluid velocity, and ϕ is the velocity perturbation potential.

In the forward problem, the following boundary conditions were applied to the plate reflecting the forward clamp and the free trailing edge (Equation 4.2).

$$w(0) = w'(0) = w''(1) = w'''(1) = 0 \tag{4.2}$$

By reversing this formulation, we provide the boundary conditions for the inverted

flag, with the fixed trailing edge and free leading edge (see Equation 4.3).

$$w(1) = w'(1) = w''(0) = w'''(0) = 0 \tag{4.3}$$

The following definition of aerodynamic pressure is substituted into Equation 4.1

$$\Delta p = \rho U \gamma(x) \tag{4.4}$$

where γ is defined by:

$$\frac{1}{2\pi}\int_0^1 \frac{\gamma(\xi)}{\xi - x} d\xi = \frac{U}{L}\frac{dw}{dx} \tag{4.5}$$

Hydrodynamic forces are assumed to be quasi steady, leading to the following simplified form of equation 4.1:

$$\frac{\partial^4 w}{\partial x^4} + \Omega^2 w + 2\kappa \frac{f(\theta) - f(0)}{\sin\theta} = 0 \tag{4.6}$$

where

$$f(\theta) = \frac{1}{\pi}\int_0^\pi \frac{\partial w}{\partial \xi}\frac{\sin^2\phi}{\cos\phi - \cos\theta} d\phi \tag{4.7}$$

and $\Omega = \omega\sqrt{\frac{\rho_s h L^4}{D}}$. Solving the eigenvalue problem shows $\Omega = 0$, substantiating the quasi-steady assumption. This contrasts the solution to the forward problem, where $\Omega \neq 0$ at bifurcation. This shows that while the quasi-assumption is valid for the inverted problem, the forward problem must consider the unsteady hydrodynamic forces. One of the key distinctions between the steady and unsteady theories is that the unsteady theory depends on the mass ratio ($\mu = \frac{\rho_f L}{\rho_s h}$) between the plate and the fluid. In the forward problem, the mass ratio exerts a strong effect on the stability of the sheet. In Kim et al. (2013), no effect of mass ratio was identified on the stability of the inverted problem. Thus, the experimental results confirm that mass ratio, and thus the unsteady theory is only important in the forward problem.

The essential result was that flapping, for an infinitely high elastic cantilever plate at zero incidence to the free stream flow begins to flap when dimensionless velocity reaches a minimum threshold of $\kappa \approx 1.85$.

4.2.1.1 Aspect Ratio

The first series of tests examined the effect of plate aspect ratio on the flapping region. A polycarbonate plate with a length of $L = 0.30$m, thickness of $h = 0.0008$m, and heights between 25mm $< H <$ 620mm was tested in the wind tunnel. Wind velocities were varied between 2.5 - 8.5 m/s at 0.5 m/s intervals. The plate was held at an angle of attack of $\theta = 0°$. Plate position as a function of time was recorded in images taken with the high speed camera at 100 frames/s. Images were processed to show a single image of the swept area of the plate during a five second duration for each of the tests. Each of the stroboscopic images formed through this process were then centered on the corresponding κ vs AR positions.

Prandtl's lifting line theory was used in order to consider different aspect ratios. This showed that plate aspect ratio has a large effect on κ. Lifting line theory gives the following governing equation:

$$\alpha(y) = \frac{\Gamma(y)}{\pi U H} + \alpha_{L=0} + \frac{1}{4\pi U}\int_{-H/2}^{H/2} \frac{\frac{d\Gamma}{dy'}}{y - y'} dy' \tag{4.8}$$

where $\Gamma(y)$ is the circulation at the position y along the chord, and $\alpha(y)$ is the geometric angle of attack. This modification led to the result that the flapping threshold given in equation 4.9 would be sufficient to excite large-amplitude flapping.

$$\kappa \approx 1.85\left(1 + \frac{2L}{H}\right) \tag{4.9}$$

4.2.1.2 Unstable Equilibrium

The previous theory was used to predict the onset of the plate flapping. A separate analysis was conducted to understand the transition from when the plate was flapping to when the plate was bent backwards. In this context, insight was gained by using the theory developed by Gosselin et al. (2010).

Gosselin et al. (2010) applies loading from hydrodynamic drag force along a beam using Euler-Bernoulli beam theory for a beam experiencing large deformation (see

Equation 4.10).

$$M = DH\frac{\partial\theta}{\partial S} \tag{4.10}$$

M is the bending moment of the beam, D is the flexural rigidity, H is the height of the plate, θ is the angle of the beam at every position along the centerline, S. Hydrodynamic loading is approximated on each section of the plate by assuming the drag force is equivalent to the force on a rigid flat plate perpendicular to the flow. This leads to the equilibrium equation:

$$\frac{d^3\theta}{dS^3} - \frac{1}{2}\kappa C_D|\sin\theta|\sin\theta = 0 \tag{4.11}$$

Solving Equation 4.11 numerically uncovers a deflected equilibrium occurring at $\kappa C_D|_{critical} = 17.62$. Consistent with the observations in Gosselin et al. (2010); Luhar and Nepf (2011), the predicted equilibrium shape matches the observed deformed shape of the plate.

Through performing a linear stability analysis on Equation 4.11, two nonzero equilibrium deflections are indicated. This indicated that there may be another stable point that occurred within the region of flapping. Through preliminary lab tests it was established that this point did in fact exist, but shedding would consistently force it away from the stable point, and flapping would resume.

To explore this concept, a pole was used to stabilize the equilibrium point. Thus, when shedding occurred, the plate was able to remain at the equilibrium position, without getting expelled from the stability region. The pole was manually guided to hold the plate at this stable position. Force was exerted by the plate if perturbed away from this position.

4.2.1.3 Phase Diagrams

The leading edge tip of the plate and deflected positions were tracked using the high speed camera and image processing tools. Data was displayed in two ways. The first looked at the horizontal displacement from the undeformed position. The second method constructed phase diagrams of the tip velocity to displacement. Since the

flapping motion occurred in the 2D plane, a nominal displacement is defined in order to avoid ambiguity (see equation 4.12).

$$\begin{aligned} u_{def} &= \int_0^L \theta(s')\,\mathrm{d}s' \\ &= \sum_{i=1}^{n} \theta(s_i)\Delta s_i \end{aligned} \tag{4.12}$$

Where $\theta(s)$ is the local deflection angle (as shown in figure 4.2). Through identifying

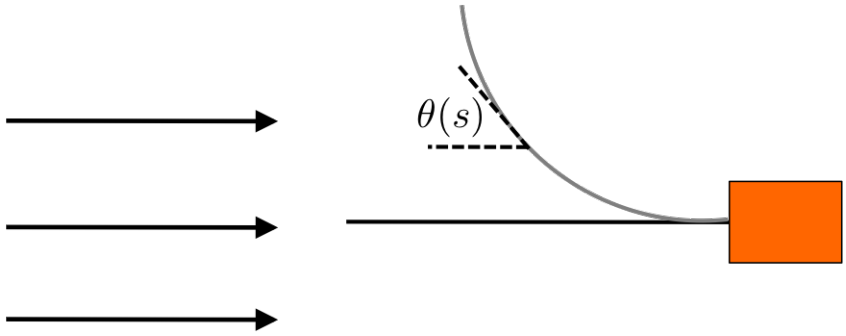

Figure 4.2. Local deflection angle $\theta(s)$

blade position through image processing, $u_{def}(t)$ was extracted for the plate during each mode of behavior.

4.2.1.4 Angle of Attack

The effect of angle of attack on flapping was also important to study in order to better understand the dynamics during a full rotation of the flapping turbine. From initial wind turbine tests, it was known that there was a range of angles of attack where flapping could occur. As with the other tests, a plate was clamped between two aluminum rods and placed in the wind tunnel. The two aluminum rods were held between optical angle selectors to allow for careful manipulation of the angle of attack. Figure 4.1 shows the plate clamped at an angle θ.

As with other tests, images were recorded with a high speed camera of the plate behavior at wind speeds between $1.8m/s < U_\infty < 8.5m/s$. During these series of

tests, the plate passed through the full range of behaviors: straight, flapping, and reconfigured. For each angle of attack the lowest flow velocity at which flapping ceased and the plate reconfigured its shape was determined.

4.3 Results and Discussion

Many variables effect the behavior of the pliable plate when subjected to a fluid flow. While Kornecki et al. (1976) showed the dimensionless parameter κ was significant, experimental tests and theory show that θ and AR are just as relevant in determining plate behavior for the inverted flag.

4.3.1 Aspect Ratio

Each of the 121 subfigures displayed in figure 4.3 were individual tests. Each test was shown visually by making a composite of 500 images, captured at 100 frames per second. The composite image was then positioned on the chart at the location corresponding to the κ and AR values of the particular test. The effect allows the visualization of the full range of movement of the plate, under a variety of boundary conditions.

The theory (see Equation 4.9) for the start of the flapping regime is compared to the experimental results and is shown by the blue line (equation 4.9). While not fitting the experimental results exactly, the general trend of aspect ratio dependence is observed. An empirical fit shows the line $\kappa \approx 1.85\left(1+\frac{L}{H}\right)$ in red as more suitable fit.

Figure 4.3 highlights that plate aspect ratio must be above a critical minimum in order for flapping to occur. It is thought that without sufficient surface area, the plate cannot generate sufficient lift to activate flapping. As aspect ratio increased above the critical minimum, flapping was observed over a wider range of wind velocities. This finding is significant, as it remains the key dissimilarity between this investigation and prior studies. Rinaldi and Paidoussis (2012) investigated an inverted elastic cylinder, which was observed to flutter but never underwent large-amplitude flapping. Alben

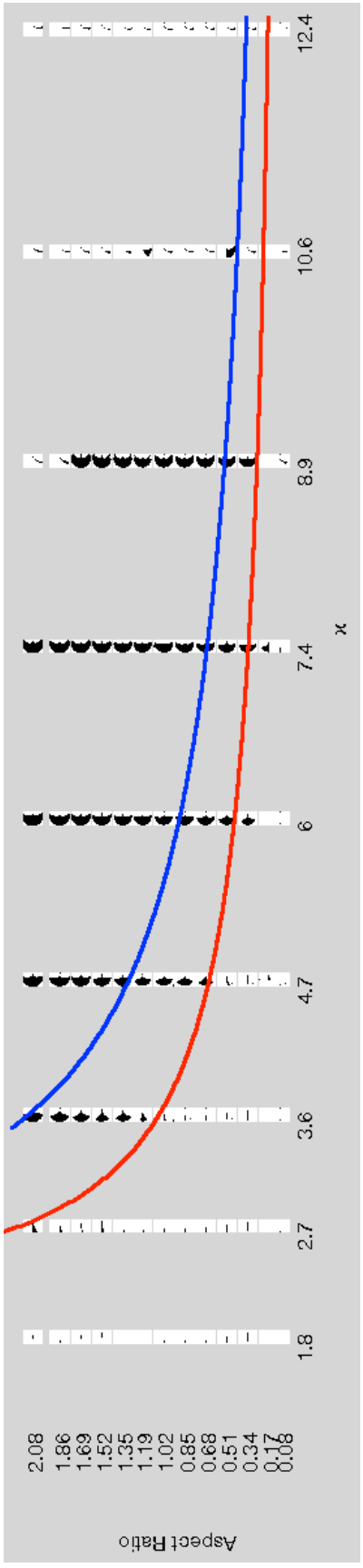

Figure 4.3. Effect of aspect ratio on flapping region. — L/H and — 2L/H

et al. (2002) experimented with 2D flows through soap visualization and silk threads. Gosselin et al. (2010) also used low aspect ratio beams in his experiments, and utilized slender body approximations in their analytical model.

4.3.2 Unstable Equilibrium

The occurrence of an additional equilibrium position was suggested by the theory John Sader developed to explain the large amplitude flapping phenomenon. Figure 4.4 illustrates the increasing angle between the plate and the free stream direction of this unstable equilibrium point as wind velocity increases.

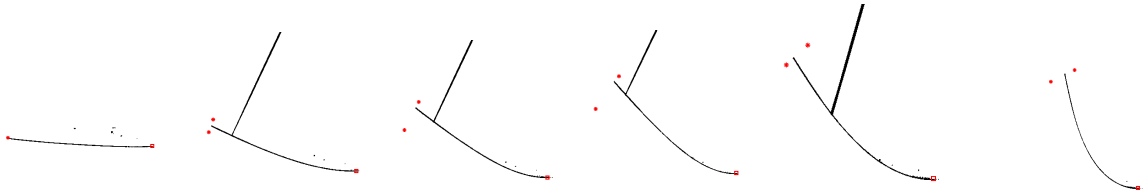

(a) 0 m/s (b) 3.5 m/s (c) 4.0 m/s (d) 4.5 m/s (e) 5.0 m/s (f) 5.5 m/s

Figure 4.4. Plate position at the unstable equilibrium. Red squares denote the clamped trailing edge and red stars mark the extreme positions of the tip from flutter.

This phenomenon was also observed physically by guiding the plate into the equilibrium state. The unstable equilibrium deflection increases with increasing wind velocity. Past a certain deformation, the equilibrium becomes stable. The pole prevented the plate from becoming unstable. However, the plate still fluttered slightly. The red stars near the tip of the plate show the range over which the tip of the plate fluttered.

4.3.3 Distinct Plate Behaviors

Kim et al. (2013) showed there were three regions: straight, flapping, and reconfigured. Further investigation shows that flapping can be classified into two varieties: periodic and chaotic flapping.

As wind speed increases, the force of drag overcomes the elastic rebounding force within the plate. This results in the plate being bent over to the side, i.e. ending up

in its reconfigured position. However, before this occurs, the large-amplitude flapping moves from being strictly periodic to unperiodic flapping. Figure 4.5 shows the plate tip location as a function of time.

This non-periodic flapping happens very close to the transition to reconfiguration and involves tuning the wind tunnel to a very narrow band of wind speeds between the two regimes of behavior.

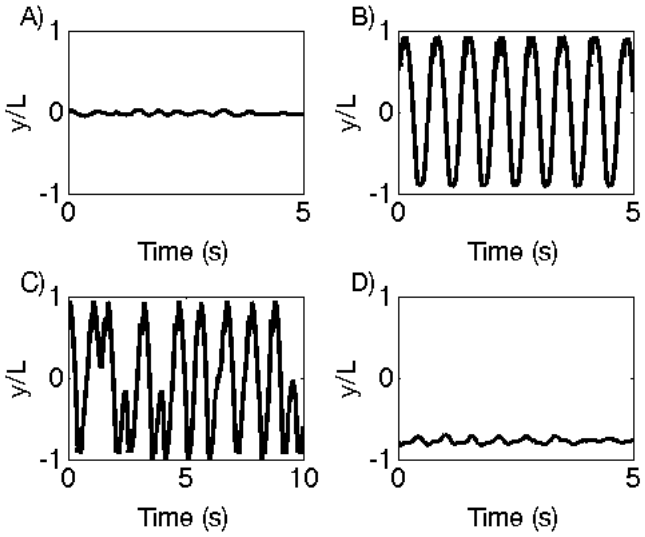

Figure 4.5. Leading edge position versus time A) $\kappa = 1.5$, B) $\kappa = 4.4$, C) $\kappa = 7.4$, D) $\kappa = 7.8$

4.3.3.1 Phase Diagrams

Figure 4.6 shows the phase diagram of the tip speed to deflection. Figure 4.6a shows the tip of a blade during a test where the plate was in the straight mode. Figure 4.6b shows the tip of a blade underling large scale flapping. Figure 4.6c shows the tip of a blade when wind velocity is sufficiently high to bend back the plate. Figure 4.6a and 4.6c show the plate tip undergoing minimal movement, indicating the plate was in a stable state. Figure 4.6b shows the dramatic movement of the tip when the plate is unstable and flapping periodically. When the chaotic flapping regime occurs, the plate bent-back past the support arms of the clamp. This blocked full visibility of the plate, preventing the more rigorous analysis required to make phase diagrams.

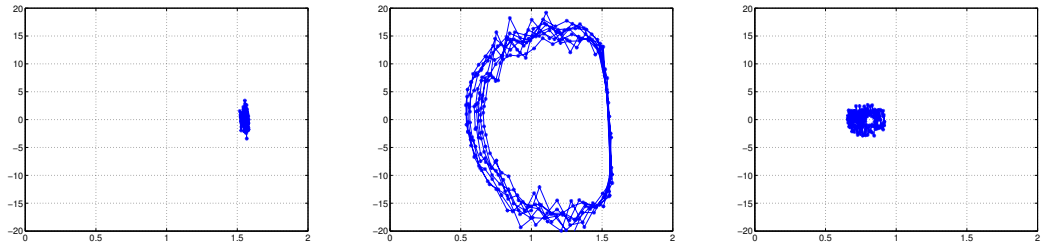

(a) a (b) b (c) c

Figure 4.6. Phase diagram between the velocity and displacement of the blade tip for a plate during (a) straight mode (b) flapping mode (c) bent-back mode

4.3.4 Angle of Attack

The effect of angle of attack was investigated because through the wind turbine studies we knew that there was a range of angles of attack where the large amplitude flapping occurred. Figures 4.7 and 4.8 compare plate behavior for angles of attack (θ) between 0° and 30°. Figures 4.7 shows the quantitative comparison of dimensionless amplitude to dimensionless velocity. In contrast, figure 4.8 shows the qualitative comparison

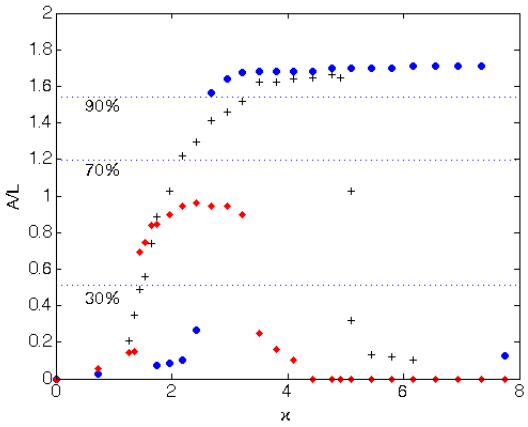

Figure 4.7. Dimensionless amplitude (A/L) versus dimensionless velocity (κ),● shows A/L for 0°, + shows A/L for 10°, ♦ shows A/L for 20°.

by displaying stroboscopic images, which provide a trace of the swept area of the plate, for each aspect ratio and velocity tested. Both figures show that the transition between the straight mode and flapping mode occurs at different wind speeds for each

Figure 4.8. Stroboscopic image of plate behavior at different angles of attack versus κ.

angle of attack. The required speed needed to achieve flapping decreases when the angle of attack increases from zero up until $\theta = 15°$. As the angle of attack increases further, the required wind velocity increases. Once the angle of attack reaches 30° the plate no longer enters the flapping region.

The wind speed at which the plate ceases flapping and enters a bent-back state decreases with increasing angle of attack. Figure 4.9 shows the lowest velocity at which the plate exhibits reconfigured behavior for each angle of attack. Results for each angle are overlaid to observe respective deformation. The bent shape of the plates is observed to be similar at the beginning of the reconfigured region for all cases. This matches the deformed shape indicated by theory to occur at the transition

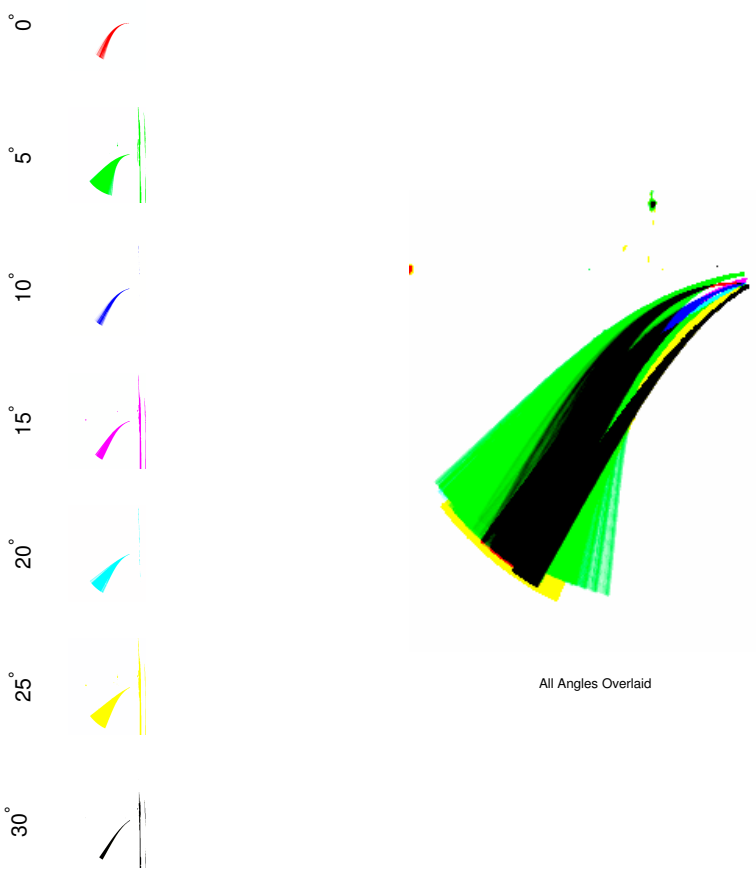

Figure 4.9. Initial configuration of plate at the first value of κ where large-amplitude flapping is no longer present. Colors correspond to Figure 4.8 to show which tests were overlaid.

from flapping to reconfigured states.

As the angle of attack changes from parallel to the fluid velocity, it becomes more difficult to separate the transition regime between not flapping and flapping. Thus a third axis was added to the chart to help describe the behavior, depending on the amplitude of flapping needed to enter the regime of large-amplitude flapping changes where this flapping regime occurs. Thus, if we take a 30% A/L as full flapping achieved, then at higher angles of attack flapping occurs more easily than in the parallel-to-wind velocity region. However, if this is insufficient to declare as full flapping amplitude, and 90% A/L is needed to claim entrance to the large-amplitude flapping regime, then higher wind velocities are needed for increasing angle of attack to enter the regime. Depending on the type of material of the flag, the range of angles throughout which flapping occurs can broaden or narrow. Regardless, large-amplitude flapping can occur over a spread of angles of attack with respect to the free stream. Figure 4.10 shows the transition between straight and flapping modes

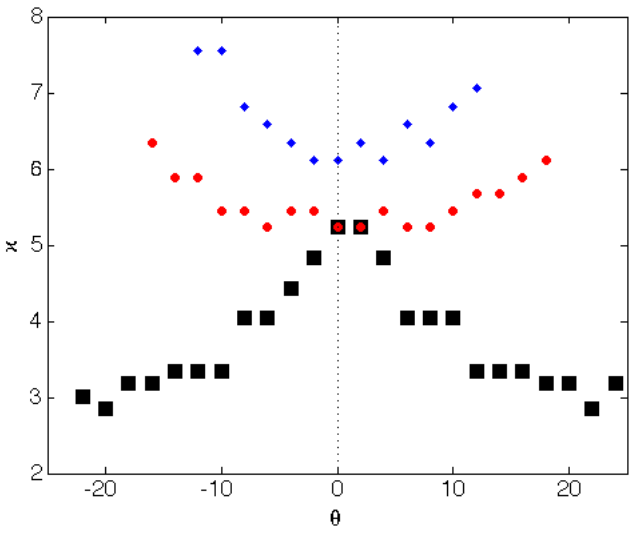

Figure 4.10. Transition velocity between straight mode and flapping mode for different angles of attack.

4.4 Concluding Remarks

Experiments and theory show the influence of angle of attack and aspect ratio on large amplitude flapping. This diverged greatly from reconfiguration, which was found to be independent of height, and thus aspect ratio. Experiments and theory lead to the following recreation of flow behavior. Figure 4.11 shows PIV images of the behavior conducted in water. When the inverted flag is held parallel to the walls of the tunnel, no lift can be created on the flat plate. Through divergence, the plate buckles, resulting in bending towards one side. Once the plate has bent towards one side, creating a small angle of attack, a vortex starts to form (Schmitz (1941)).

The separation bubble reduces pressure which increases lift, pulling the plate further away from the initial configuration. At all times, lift and elasticity are in balance: as lift increases the plate bends back, creating a larger but balanced elastic force. When the separation bubble sheds and is carried away downstream the lift force drops. The elastic force is no longer balanced by the lift force, so the plate rebounds back towards the initial configuration. The plate will start to form a new vortex as it rebounds past center line ($\theta = 0$) towards the opposite extreme and the process restarts.

Large amplitude flapping occurs over a narrow band of non-dimensional bending stiffness, at large enough height of plates, and throughout a range of angles of attack. Due to the nature of prior reconfiguration studies, this regime had not been entered during experimental testing prior to the wind turbine tests. This regime of flapping is incredibly sensitive to boundary conditions. However, through repeated experiments performed by various experimenters (Daegyoum, Cecilia, and myself) we do know conclusively that the experimental range does exist. Thanks to John Sader's theory we have shown that the instability is largely lift driven, and occurs until the point where drag overcomes the balance between lift and elastic forces of the plate. Once drag becomes a deciding force, the plate once again leans towards reconfiguration.

Etnier and Vogel (2000) likely entered a region where drag force was dominate, resulting in the twisting of a highly flexible daffodil stem. If the dimensionless bending

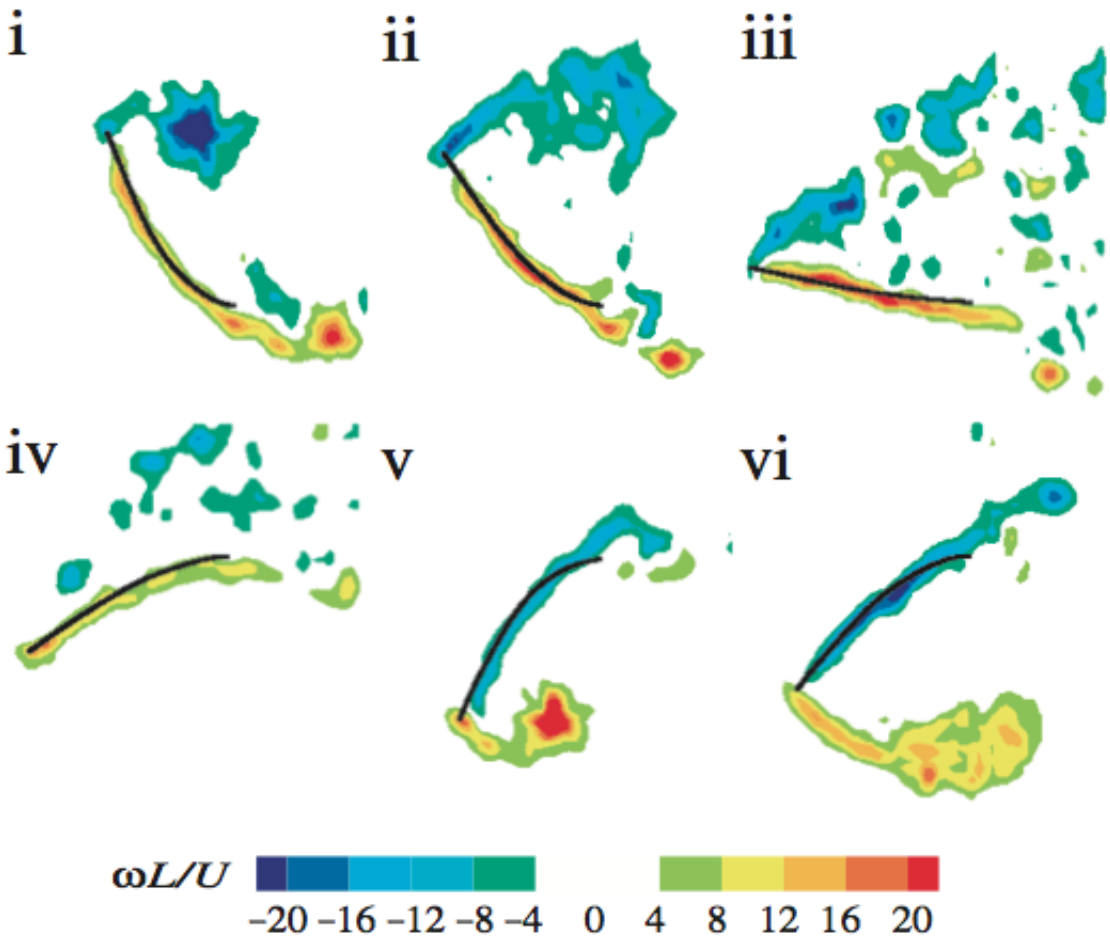

Figure 4.11. Vortex Shedding & Plate Flapping

stiffness is low enough, the body could pass through the flapping regime without flapping and enter into the better understood reconfiguration regime.

Reconfiguration is a useful mechanism used by plants to help prevent damage in storm conditions by reducing the force loads acting on the plant. In contrast, the large-amplitude flapping mechanism increases the drag coefficient (Kim et al. (2013)). This aids the propulsion of the flexible blade vertical axis wind turbine discussed in Chapter 3.

Chapter 5

Vertical Axis Wind Turbine: Caltech FLOWE Testing

5.1 Introduction

The Caltech Field Laboratory for Optimized Wind Energy (FLOWE) is a unique environment, primarily set up to investigate array spacing of vertical axis wind turbines in real wind conditions. As such, the Caltech FLOWE offered the perfect setting to test the concept of a flexible blade wind turbine at full scale, and to evaluate the rotor performance as well as its durability. Furthermore these first tests provided the necessary feedback in order to iterate the turbine design with regard to the generator and inverter. While experiments at FLOWE are ongoing, this chapter explores the preliminary findings and challenges.

5.2 Materials and Methods

5.2.1 Windspire^{TM} turbine base

The Caltech FLOWE currently uses several Windspire^{TM} turbines from Ark Alloy, LLC in the VAWT array studies. Windspire^{TM} produces a unique wind turbine base that includes the generator and inverter in the design. The base includes a dual bearing mechanism that prevents lateral loading from perturbing the alignment of the vertical shaft. The base structure has one bearing located at the base and one

near the top of the tower just below the generator. By spacing the bearings in such a way, the vertical axis is stabilized against the lateral loading by the wind, preventing lateral forces from perturbing the alignment of the rotor and generator. Alignment is critical in order to avoid friction losses. Using the Windspire^{TM} base and fitting the new flexible blade rotor design to it allowed for rapid testing of the prototype.

Figure 5.1 shows a mock up of the turbine rotor on Solidworks done by Lutz Müller. The central axis can be equipped with up to four rotor blades. The model in Figure 5.1 shows two blades, while a configuration with three blades was used in the field test.

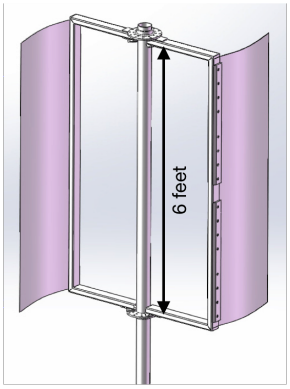

Figure 5.1. Solidworks model of field site VAWT rotor

The Windspire^{TM} turbine has hinges on the bottom of the base that allow easy raising and lowering of the turbine. Figure 5.2a shows the turbine lowered on the hinges during initial installation of the prototype. Figure 5.2b shows the turbine in its upright position after the initial assembly was completed on July 29, 2013. The rotor had 1/32 inch thick Delrin blades attached. The turbine was released into winds ranging between 7 and 15 ms^{-1}.

5.2.2 Data Collection

As expected, the rotational speed of the flexible rotor design is significantly lower than it was for the original lift based Windspire^{TM} rotor. This results in a lower voltage output by the turbine's generator. Unfortunately the voltage output was so

(a) Turbine lowered during rotor installation

(b) Turbine with 1/32 inch thick Delrin blades installed. Image courtesy of davidkremers

Figure 5.2. First tests at field site: July 29, 2013

low that neither the Windspire^{TM} nor the Aurora PVI-3.6-out-w-us inverters were able to extract power from the generator.

The installed Windspire^{TM} generator provides an output voltage that is linearly related to the rotational speed of the turbine. In order to obtain rotational speed, a voltage divider was jury-rigged, bringing the output voltage from the generator down sufficiently to be compatible with the input range of the National Instruments USB-6211 DAQ card. Figure 5.3 shows the iterations of voltage dividers built.

In order to measure the rotational speed of the rotor, a hall effect sensor was later attached to the turbine and fed into LabVIEW through the same National Instruments USB-6211 DAQ card. By measuring the generator output voltage and the rotor RPM through the hall effect sensor signal simultaneously, the calibration curve for the linear relationship between the two quantities was obtained.

In order to achieve a wide range of rotational speeds, the turbine was manually stalled. By attaching a hall effect sensor to the turbine, and measuring both the generator output voltage and the RPM simultaneously, while manually stalling the turbine and slowly releasing the turbine, we were able to obtain a calibration curve

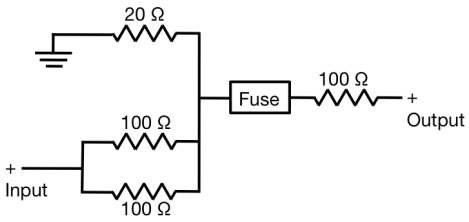

(a) Voltage Divider Schematic

(b) Lab Bench Voltage Divider

Figure 5.3. Voltage Divider

for the generator output voltage to the turbine RPM as shown in Figure 5.4.

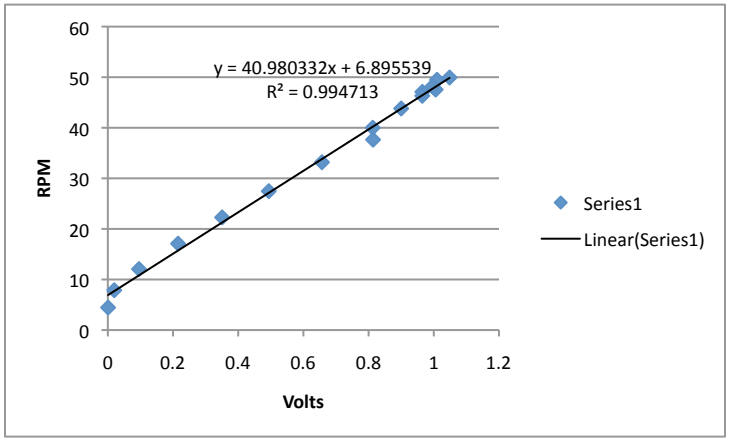

Figure 5.4. Calibration of wind spire generator voltage to RPM output. RPM measured by a hall effect sensor.

5.3 Results and Discussion

Three blade materials have been tested at the site so far: Delrin, rubber, and stainless steel 301 (see table 2.2). Rotational speed and wind velocities at the site were compared where reliable data was obtained.

5.3.1 Windspire^{TM} base - RPM & Fatigue testing

5.3.1.1 Rubber Blades

Rubber blades were installed on August 12, 2013. Figure 5.5 shows the turbine with rubber blades installed. At this point the data acquisition system, which was

Figure 5.5. Flexible blade turbine with rubber blades.

recording rotational velocity of the rotor, was running stably. Figure 5.6 shows the comparison of wind velocity to rotor speed.

Notably, there are several time segments during which the turbine stopped rotating. These events correspond to low wind velocities that often occur at FLOWE during the night. This allowed for a rough estimate of the cut in speed for this particular turbine configuration. The RPM data was analyzed to find each time frame where rotation ceased. From there, the next point at which rotation resumed was found, and the wind velocity at this point in time stored.

Using the velocity data for all the points in time at which the turbine started from rest allows allows us to make an assessment of what the cut in speed is.

This method is imprecise due to the wind measurements averaged over a ten minute interval, but it does allow for a rough idea of what an expected cut in speed might be. The cut in wind speed is determined as the maximum value of all the wind

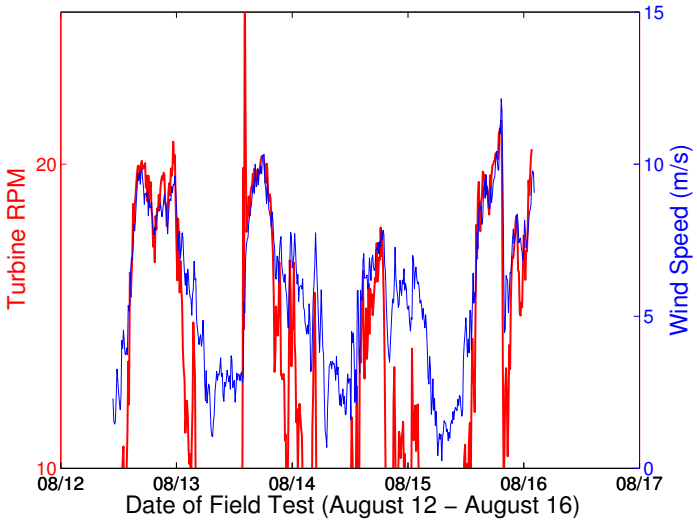

Figure 5.6. Comparison of turbine RPM to wind velocity at the Caltech FLOWE.

speeds recorded when the rotor started spinning from rest. For the rubber blades the cut in speed was found to be 5.6 m/s.

Another set of experiments was done at the field site using a hall effect sensor. The hall effect sensor was primarily used to calibrate the voltage output from the Windspire^{TM} generator. However, it also provided a way to look at the turbine rotational speed more closely. Figure 5.7 shows a sequence of rotations displaying both the data from the hall effect sensor (black vertical lines) and RPM calculated from the generator voltage (red curve) for a period of time when the 10 minute wind averages were between 9.9 to 11.1 m/s. The hall effect sensor marks each time the

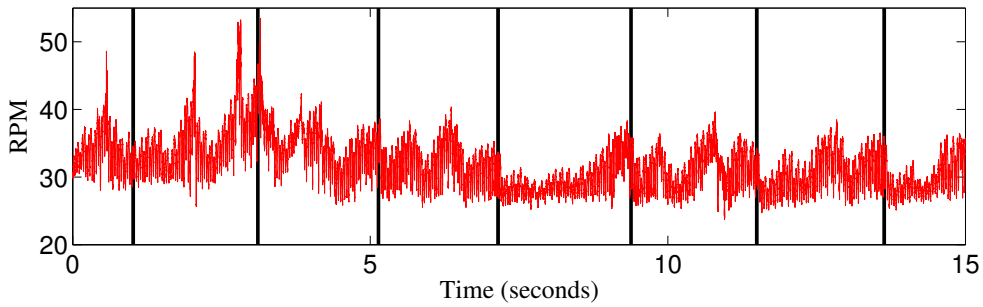

Figure 5.7. Close up of rotational speed of turbine with rubber blades.

turbine completes one full rotation, as noted by a black vertical line in Figure 5.7. Three peaks and valleys are observed in the rpm data between each of the black vertical lines, showing a local velocity and power peak each time one of the three blades captures the wind. This matches the behavior seen in the wind tunnel. The power impulse created by the blade slowly fades out as the next blade passes into the propulsion section of rotation, generating its own impulse to the turbine.

Wind conditions change rapidly, primarily due to gusts, which aren't captured by the wind speeds recorded at 10 minute intervals. However, the gusts can be observed by looking closely at the inconsistent rising and falling of rotational speed not attributed to the blades' position.

5.3.1.2 Stainless Steel 301 Blades

On September 20, 2013, high fatigue strength stainless steel blades were installed on the turbine, replacing the rubber blades. Figure 5.8 shows the turbine with these blades.

Figure 5.8. Flexible blade turbine with stainless steel blades.

Figure 5.9 shows the comparison between turbine rotor rpm and wind speed for this blade configuration and wind speed for the study. As with the rubber blades,

comparison between the turbines rotor velocity and the wind speed allowed for an estimation of the cut in speed. The cut in speed found through the analysis described above shows that the cut in speed is between 4.3 - 5.0 m/s. Not only is the cut in speed of the rotor lower for the steel blade configuration but the rpm achieved at a given wind speed is higher compared to the rubber blades.

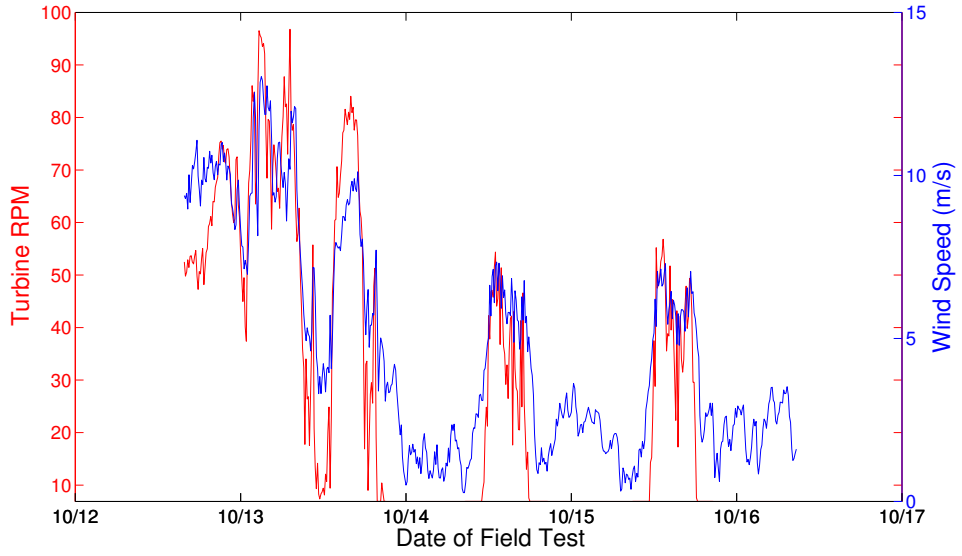

Figure 5.9. Turbine RPM (red) and wind speed (blue) over time for the turbine configuration with the steel blades.

5.3.2 High torque/low RPM generator testing

The Windspire^{TM}generators were unsuitable to generate power due to the torque output of the flexible blade rotor being considerably higher than predicted, and the rotational speed significantly lower than expected. As a result, the flexible blade turbine rotor was transferred to a high torque low RPM generator on October 16, 2013. Figure 5.10 shows an image of the turbine installed on the new generator placed on top of a wood tower. The wood tower is a 40-feet high utility pole with a 1-foot diameter. The lowest eight feet of the tower is sunk into the ground and secured by a gravel and concrete foundation.

Figure 5.10. Stainless Steel Blade Turbine on high torque generator.

The generator was connected to the Aurora inverter and the power curve supplied by the manufacturer (Xinda Green Energy Co. Ltd.) was programmed into the inverter. Unfortunately, October 16th, 2013 was a windless day and therefore the power curve couldn't be adjusted to the torque production of the flexible blade rotor. Therefore, the applied power curve didn't allow the rotor to spin and the turbine blades were damaged by October 29, 2013.

The wind farm typically experiences wind shortfall between November and February; thus further testing was delayed until winds picked back up in the spring.

5.3.2.1 Delrin Blades: Wind Turbine Damage Comparison

While the ultimate goal of this project was to design a turbine that could withstand high winds, the initial prototype sustained damage within the first two weeks of testing. In addition, a Windspire^{TM} turbine that was approximately 215 feet away was also damaged at the same time. This allowed for a comparison of maintenance costs between the flexible blade wind turbine and the Windspire^{TM} turbines that are tested at FLOWE. Figure 5.11 shows (a) the flexible blade wind turbine and (b) the

Windspire^{TM} turbine damage sustained during the same timeframe.

(a) Flexible Blade Wind Turbine

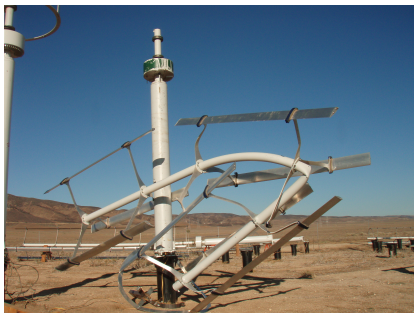

(b) Windspire Turbine

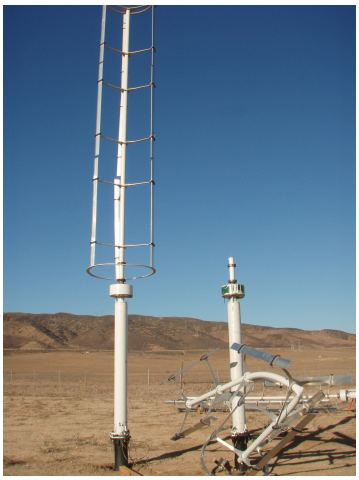

(c) Windspire Turbine

Figure 5.11. Damage Comparison: August 12, 2013

In both cases the turbine rotors were damaged. However, the flexible blade wind turbine simply lost several of its blades, i.e. the material sheared off right behind the position where the blades are clamped to the rotor structure. On the other hand, the Windspire^{TM}rotor sheared completely off its connection to the main vertical shaft, resulting in collapsed and deformed rotor and blades. This damage pattern has been observed at similar events at FLOWE before. In this way, the flexible blade wind turbine can be likened to a tree losing several leaves and minor branches in a storm. The implication is that by allowing for minor damages, the essential form remains standing – in this case the full rotor structure, base, and generator.

In the case of the flexible blade wind turbine, it was possible to replace the turbine blades within 0.5 man-hours, quickly restoring the turbine to operational conditions. In comparison, the Windspire^{TM} turbine required eight man hours prior to becoming functional.

While a cost comparison of repairs and parts is difficult to perform due to the experimental nature of the site, table 5.1 shows the estimated cost of damage repair for this event. Cost of replacement parts for the flexible blades are artificially inflated as a result of expedited machining. In addition, labor costs are difficult to separate

between the repairs and the ongoing work at the site. Labor costs are estimates based on contractor wages and not representative of actual payment. Nevertheless, table 5.1 attempts to provide ballpark figures of repair costs. Costs also neglect downtime of the turbines and lost power output.

Table 5.1. Cost Analysis of Turbine Repairs

	Flexible Blade Turbine	Windspire™
Manual Labor	0.5 man-hours	8 man-hours
Cost Labor	\$100/hour	\$72.5/hour
Total Cost Labor	\$50	\$580
Cost Replacement Parts	4 Blades x(\$29-\$37/Blade)	4 x Blades \$40/Blade 1 Clamp x \$35/Clamp 15 Struts x \$20/Strut 1 x \$750/Rotor Shaft
Total Parts Cost	\$125	\$1245
Total Cost	\$175	\$1825

Repair costs of the Windspire™ turbine are significantly higher than the repair costs of the flexible blade wind turbine. In large part, this cost stems from replacing the rotor shaft, which is comparatively expensive due to the tight tolerances required during manufacturing. Because the blades ripped off the flexible blade turbine, the base and essential parts of the turbine were left unharmed.

Figure 5.12 shows the wind velocities recorded as 10 minute averages at the field site throughout the test period, during which the damage seen in Figure 5.11 occurred.

Even though the wind velocities exceed the Windspire™ cut out value of 12m/s they are not critically high. Since two different turbines were damaged during the same time period, it seems likely that there was a high wind event. However, Figure 5.12 doesn't appear to support this. While it's true that the two turbines could have been damaged due to individual defects, it is more likely that a wind gust was responsible. Since the wind speed is recorded in 10 minute intervals, the averaging would moderate the appearance of gusts.

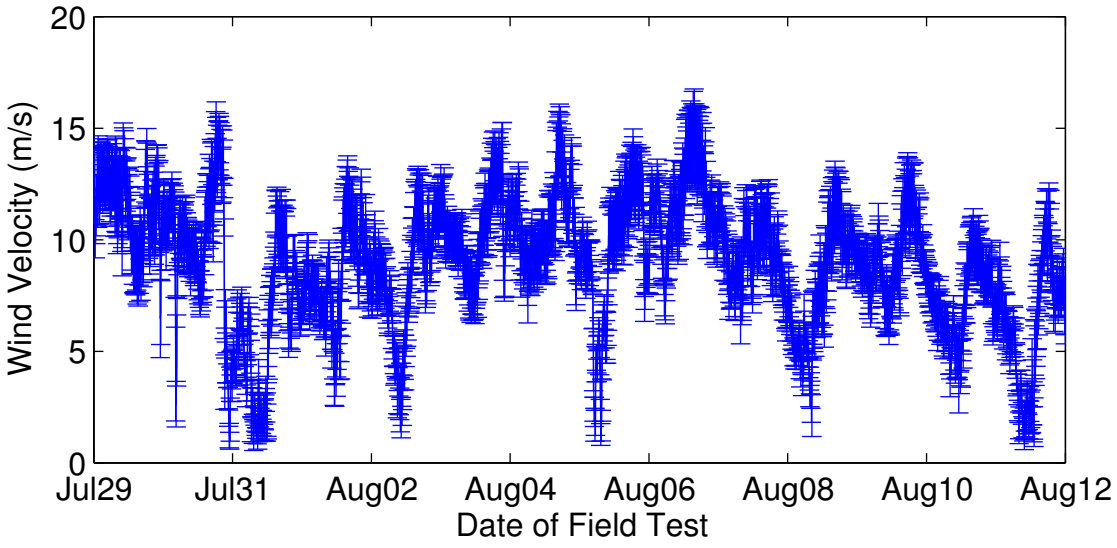

Figure 5.12. Wind speeds given at 10 minute averages for period of delrin 1/32nd blade testing

5.4 Concluding Remarks

Field testing has proven to be considerably more challenging than wind tunnel testing, primarily due to our reliance on Mother Nature to provide adequate testing conditions. However, moving from the lab to the field proves that the flexible blade concept also works at large scales and provides a realistic assessment of the technology. However, the preliminary results at the field site are encouraging in that the rotor design shows promise, and produces similar flapping behavior to those observed in the wind tunnel studies of the rotor design. Flexible, replaceable blades have proven to prevent expensive damage.

The tests are ongoing with a new generator currently set up for testing. More detailed testing, especially with regard to power production, will be conducted. This work is left for the future when the winds pick back up at the field site. It will focus on implementing high torque low rpm generators.

Furthermore, wind velocities averaged over 10 minutes intervals are not detailed enough to obtain the information needed to properly characterize a new turbine type. The wind sensor set-ups have been changed to also record the wind speed with a

frequency of 1Hz.

Chapter 6

Summary and Future Works

The work described in this thesis successfully implements flexibility in a proof-of-concept design of a vertical axis wind turbine, both as a model in a wind tunnel and at full scale at a field site. The work uncovered a new flapping instability, which became the focus of further experiments. While this thesis adds to the understanding of pliable plated behavior and includes several thought-provoking applications, there is always more to discover. The experiments presented in this thesis provide the first examination of what underlying mechanisms influence the occurrence of flapping in an inverted flag configuration.

6.1 Vertical Axis Wind Turbine

A vertical axis wind turbine was designed and a model was analyzed in a wind tunnel. Subsequently, a full scale model was deployed and tested at the Caltech FLOWE. The idea behind the flexible blades is to use reconfiguration of the material to increase drag on the power-producing side of the VAWT rotation and decrease drag when the blade is moving against the wind. In the wind tunnel, the model turbine was tested with blades featuring a wide variety of stiffness. The stiffest blades prevented the turbine from rotating, due to the symmetry on either side of the turbine. When the pliable blades were affixed to the turbine, the turbine was able to rotate and produce work against the load applied to the turbine. Large-amplitude flapping of the 1/32 inch-thick Delrin blades was observed as the blade moved downwind. Further experiments

focused on this finding in an attempt to understand the mechanisms behind the flapping.

In addition to the experimental testing of the VAWT in the tunnel, an analytical model was used to understand the impact of reconfiguration. The rubber blades, which were observed to undergo reconfiguration, and the stiffest aluminum blades were compared to the analytic solution. As predicted, reconfiguration was shown to be responsible for the torque differential created by the turbine with rubber blades affixed, and showed that rotation would be prevented due to the geometry when aluminum blades were affixed.

The field site experiments are still underway, currently waiting for winds to regain full strength in order to continue the field investigation of the wind turbine. Ultimately, the flexible blade VAWT showed remarkable characteristics, and was easily self starting when released into the winds. In addition, while blade durability is low, disposable blades prevented catastrophic turbine damage from occurring during a high wind event. Of primary interest is the finding of an appropriate generator and inverter combination that matches the torque and RPM of the rotor, and thus produces electricity which could be fed into the grid. While this thesis has focused on the aerodynamics of wind turbine blades, rotor dynamics are only a small aspect of a functioning wind turbine (Hau (2006)). Furthermore, the influence of additional blades on the torque generated by the rotor will be examined.

The commonly used ten-minute averages of wind velocity data do not provide enough information to analyze precise turbine behaviors. Changing the set-up to capture wind velocity during a shorter time scale would allow for stronger correlation between velocity and turbine behavior. Recently, steps have been made to record wind velocities at the field site at intervals of 1Hz.

While the current VAWT uses passively actuated blades, actively controlled blades have also been considered. Appendix A describes one concept for implementing actively controlled blades to the vertical axis wind turbine.

6.2 Flapping Plate Behavior

To gain a better understanding of the dynamics of the flexible blades, the large-amplitude flapping of an elastic plate was studied experimentally in a wind tunnel. The experiments show that large amplitude flapping only occurs in a narrow band of dimensionless velocity (κ). The limits of this band depend on both the aspect ratio of the plate and the initial angle of attack of the plate to the free stream. Large-amplitude flapping is only observed above an aspect ratio of 0.15. In addition, the flapping starts to occurs at lower wind speeds as the angle of attack increases from incidence to approximately 15°. The flapping starts at increasing wind speeds as the angle of attack of the plate further increases from 15° to 25°. Ultimately, the plate stops flapping around 30°. The plate stops flapping and enters a reconfigured state at roughly the same deformation across all angles of attack tested. The experiments also indicate the existence of an unstable equilibrium point. This unstable equilibrium point is found to increase with increasing wind velocity until flapping no longer occurs.

Current studies have focused on the flapping occurring at a Reynolds number of 10^5. Further studies are underway to investigate the plate behavior at the lower Reynolds numbers, i.e. 10^4. In order to conduct tests at lower Reynolds number, a new, smaller, and thinner clamping device will be built. This new clamp will also aid in addressing whether or not the discrepancies between theory and experimental onset of flapping are due to the clamp's size and shape. In addition, the clamping mechanism can be further modified to avoid blocking the camera's view of the plate within the chaotic flapping region. This would allow for a more rigorous phase diagram of this particular plate behavior.

Additional studies could also focus on how the elastic plates behave in different array configurations of several similar plates. The current experiments solely investigated rectangular plates, however, further experiments could also focus on the shape profiles of the elastic plates.

Appendix A

Shape Morphing through Internal Pressure

There are a few different shape-morphing mechanisms currently in use, such as shape memory alloys and piezoelectric materials. Here, initial tests investigated the use of hydro-skeletons as an alternative method of shape morphing to eliminate the need to generate substantial voltage and temperature differences. Figure A.1 shows a device bending while internal pressure increases. The idea behind this shape-morphing

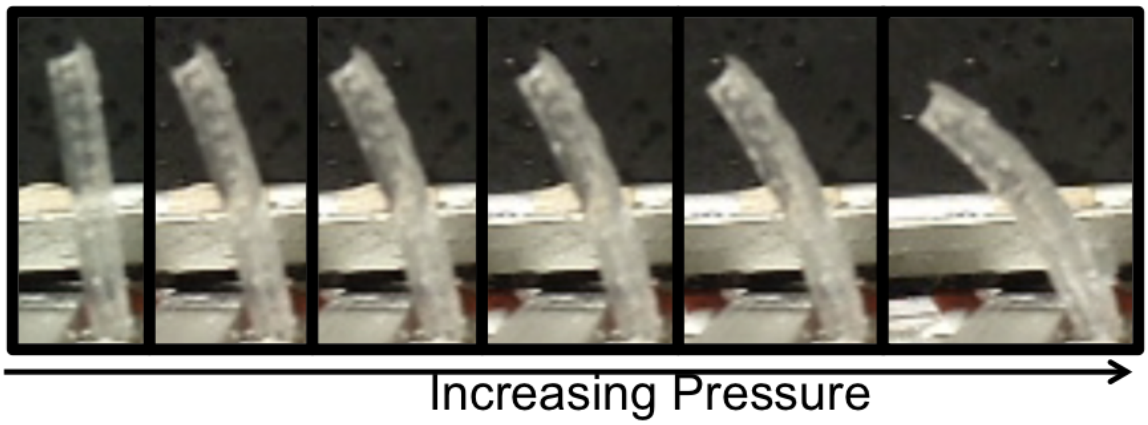

Figure A.1. PDMS device bending due to increasing internal pressure.

mechanism is to bond two dissimilar materials to each other with an internal chamber embedded between them (Shepherd et al. (2011)). Through pressurization of the internal chamber, the device will bend away from the more elastic material (see figure A.2).

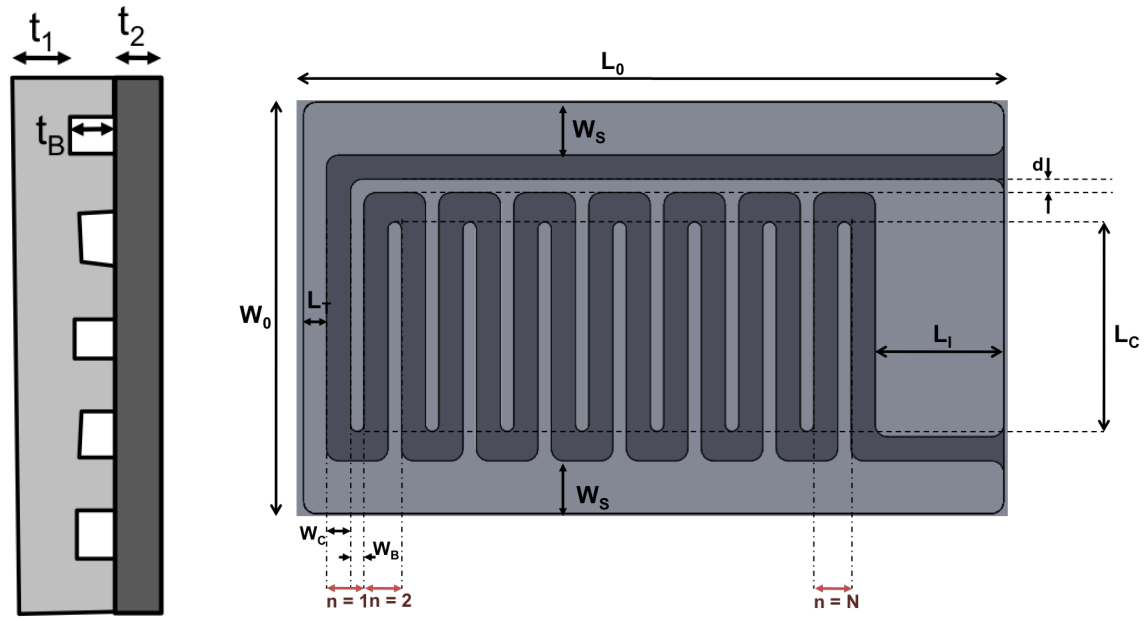

(a) Side View (b) Front View

Figure A.2. Geometry of Shape Morphing Structures

Initial experiments focused on changing the drag of a plate through bending of the devices. Figure A.3 shows the (a) side view and (b) frontal view of the experimental setup of an aluminum plate with devices attached to the top of a stiff aluminum plate. By increasing the pressure of the internal chamber, the device bends, changing the tip characteristics of the plate.

Figure A.4 show the preliminary results recorded of the small change in drag force due to the shape morphing of the plate tip. Ultimately, small changes in the tip shape change the drag the plate experiences. However, further work on stabilizing the internally pressurized devices is necessary to prevent rupture of the devices when pressurized. Following improved performance of the devices, actively controlled blades using this technique could be applied to the flexible blade vertical axis wind turbine.

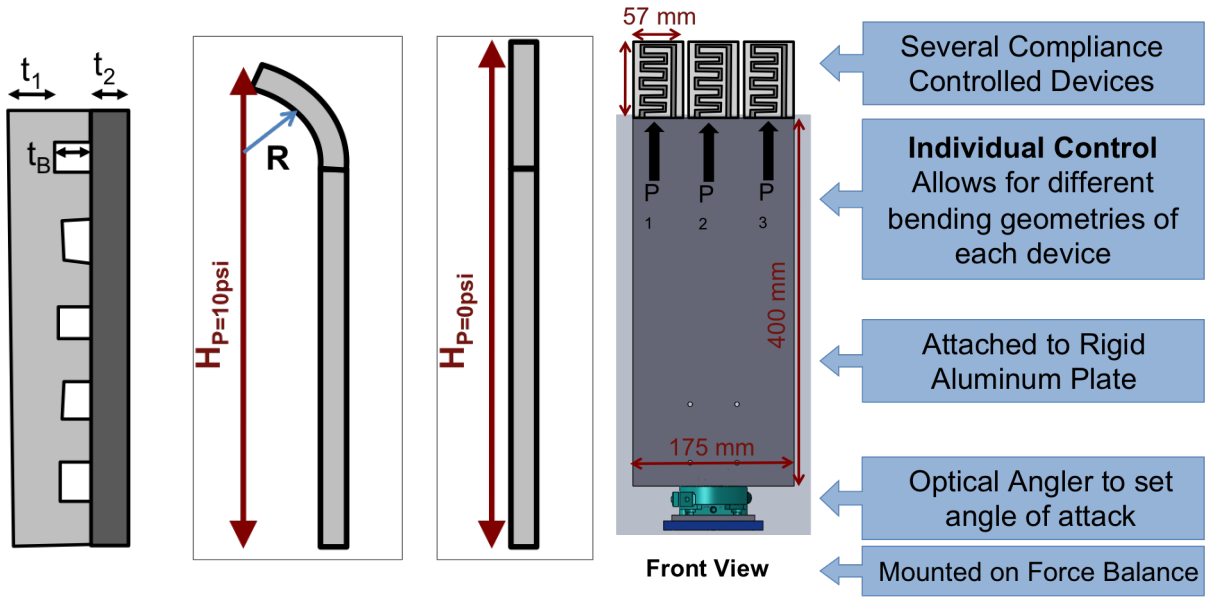

(a) Side View (b) Front View

Figure A.3. Experimental setup of an internally pressurized device attached to the top of a stiff plate.

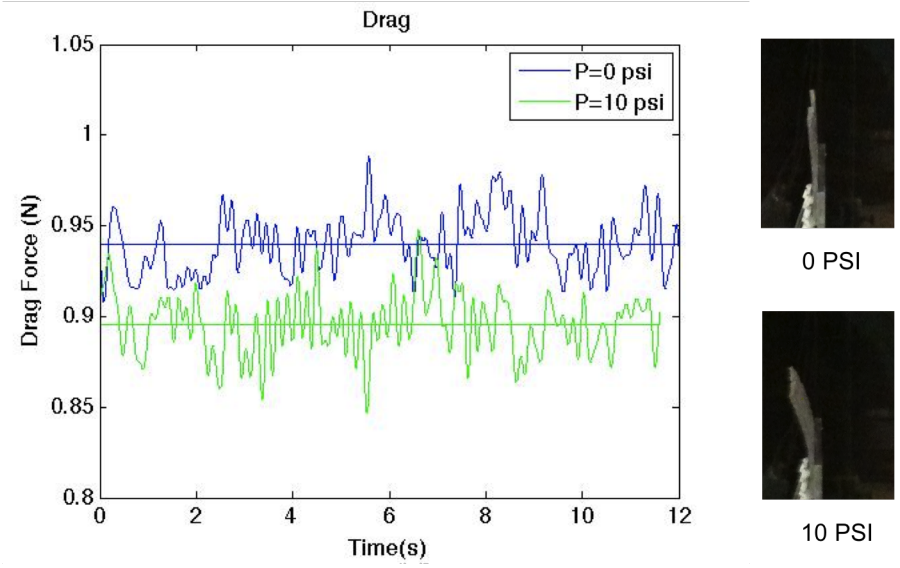

Figure A.4. Preliminary results demonstrate change in forces due to shape morphing plate tip.

Appendix B

Image Processing

B.1 Image Processing Set-Up

First, images are cropped appropriately to reduce the field of view to the area where the flapping cantilever occurs. This allowed the frame to be cut out of the image and allowed for automatic image processing.

For each series of tests, image cropping was done manually. Once an appropriate crop had been found for the series, it was used throughout.

B.2 Image Processing Scripts

B.2.1 Tip Tracking

```
close all
clear all
clc

%Define Image Crop
WIDTH=450;
HEIGHT=280;
RECT=[90 70 WIDTH HEIGHT];
```

```
%values from no-wind data
lengthpix=222;%max(iimax)-min(iimin)
centerline=221;%mean([max(jjmax) min(jjmax)])
x_zero=221;
y_zero=40;
xp_zero=227;
yp_zero=262;
v_zero_x=xp_zero-x_zero;
v_zero_y=yp_zero-y_zero;

camera_frequency=207;

oput_dir='/Users/Julia/Documents/Professional/Caltech/Reverse Flapping - Angle of
oput_fmt='.tif';
start=7898;

n=300; % number of pictures to analyze
FR=100;
alpha='A';

% vidObj=VideoWriter(vid_name);
% vidObj.FrameRate=FR;
% open(vidObj);

for g=1:n

        IM=imread(num2str(strcat(oput_dir,'0000',num2str(start),oput_fmt)));

%     [x,map]=gray2ind(IM);
%     img = ind2rgb(x,map);  %# Convert image 1 to RGB
```

```
%     lev=graythresh(img);
%     BW=im2bw(img,lev);
%     image(BW)
%     image1=img;%
     %zoom on
    image1=imcrop(IM,RECT);
    start=start+1;

    %IM=wiener2(IM,[10,10]);

    BW1=edge(image1,'sobel');

    se90 = strel('line', 5, 90);
    se0 = strel('line', 3, 0);
    BW1 = imdilate(BW1, [se90 se0]);

     %imshow(image1)
     %hold on


%     [B,L,N]=bwboundaries(BW1)

    boundaries = bwboundaries(BW1);
    numberOfBoundaries = size(boundaries);
    for k = 1 : numberOfBoundaries
        thisBoundary = boundaries{k};
        sizeBoundary(k)=length(thisBoundary);
    end
    Lmax=max(sizeBoundary);
    kk=find(sizeBoundary==Lmax);
```

```
    tB=boundaries{kk};
     %plot(tB(:,2), tB(:,1), 'g', 'LineWidth', 2);

    %hold off
    clear sizeBoundary

    for m=1:length(tB)
        x_try=tB(m,2);
        y_try=tB(m,1);
        d(m)=sqrt((x_try-x_zero)^2+(y_try-y_zero)^2);
    end
    dMAX(g)=max(d);

    IND_of_tB=find(d==max(d));
    IND_end(g)=IND_of_tB(1);
    clear d
    pix_END(g,:)=tB(IND_end(g),:);
     %plot(tB(IND_end(g),2),tB(IND_end(g),1),'ro')
%
%     plot(xp_zero,yp_zero,'xr')
%
     %hold off
%
%     pause(0.1)

    vp_x=tB(IND_end(g),2)-x_zero;
    vp_y=tB(IND_end(g),1)-y_zero;

    u = [vp_x vp_y];
    v = [v_zero_x v_zero_y];
```

```
    xsign=v_zero_x-vp_x;
    CosAngle = dot(u,v)/(norm(u)*norm(v));
    AngleInDegrees(g) = acos(CosAngle)*sign(xsign)*180/pi;


   % image(image1)
    %axis equal
    %axis off

%

%     currFrame=getframe(gcf);%,[15 10 540 400]);
%     pause(0.1)
%     writeVideo(vidObj,currFrame);
%
%      g
end
% close(vidObj);
lengthpix=222;%max(iimax)-min(iimin)
centerline=221;%mean([max(jjmax) min(jjmax)]) %4.5 inches
pix_END
ymax=max(pix_END(:,2))-centerline
ymin=min(pix_END(:,2))-centerline
ymin_per_L=ymin/lengthpix;
ymax_per_L=ymax/lengthpix;


time=[1:n]/camera_frequency;

%figure(2)
```

```
%plot(time, AngleInDegrees)

[pks pklocs]= findpeaks(AngleInDegrees,'minpeakdistance',70);
npeaks=size(pklocs)
NegAngle=-1*AngleInDegrees;
[negpks negpklocs]=findpeaks(NegAngle,'minpeakdistance',70);
negnpeaks=size(negpklocs)

if npeaks(2)>1
    frequency=camera_frequency*(npeaks(2)-1)/abs(pklocs(1)-pklocs(npeaks(2)))
elseif negnpeaks(2)>1
    frequency=camera_frequency*(negnpeaks(2)-1)/abs(negpklocs(1)-negpklocs(negnpea
elseif npeaks(2)==1 & negnpeaks(2)==1
    frequency=camera_frequency/(2*abs(negpklocs(1)-pklocs(1)));
else
    frequency=0
end



Amplitude=0;

if negnpeaks(2)<npeaks(2)
for ii=1:negnpeaks(2)
Amplitude=Amplitude+pks(ii)+negpks(ii);
end
Amplitude=Amplitude/negnpeaks(2)
else
for ii=1:npeaks(2)
Amplitude=Amplitude+pks(ii)+negpks(ii);
end
```

```
Amplitude=Amplitude/npeaks(2)
end
```

Appendix C

Turbine Blades Reconfiguration Model

Using the same theoretical framework as Gosselin et al. (2010), we start with the equation for the bending moment in a beam given by Euler-Bernoulli beam theory (Equation C.1).

$$M = DH\frac{\partial\theta}{\partial S} \tag{C.1}$$

where M is the bending moment of the beam, D is the flexural rigidity, H is the height of the plate, θ is the angle of the beam at every position along the centerline, S. The drag force exerted on the beam is given by:

$$F_D = \int_0^L -\frac{1}{2}\rho H C_D^R (U\sin\theta)^2 \sin\theta dS \tag{C.2}$$

where C_D^R is the drag coefficient on the rigid blade. The following dimensionless variables are used to find the non-dimensional Equations C.4.

$$\Re = \frac{F_D}{\frac{1}{2}\rho H L C_D^R U^2}$$

$$\widetilde{C_y} = C_D^R \frac{\rho L^3 U^2}{2D} \tag{C.3}$$

$$\frac{\partial^3\theta}{\partial S^3} = -\widetilde{C_y}\sin^2\theta$$

$$\Re = \int_0^1 -\frac{\sin^3\theta}{\sin^3\theta_0} ds \tag{C.4}$$

These equations are solved for each blade numerically, for the appropriate material and wind conditions. After $\Re$ is found, the force exerted on the plate is obtained through Equation C.4. Once the force on both blades is obtained, the net torque (τ on the turbine is obtained through Equation C.5.

$$\tau = r * (F_{D1} - F_{D2}) \tag{C.5}$$

where r is the distance of the base of the blades from the center of the vertical axis.

Bibliography

Akcabay, D. T. and Y. L. Young (2012, May). Hydroelastic response and energy harvesting potential of flexible piezoelectric beams in viscous flow. *Physics of Fluids 24*.

Alben, S., M. Shelley, and J. Zhang (2002, December). Drag reduction through self-similar bending of a flexible body. *Letters to Nature 420*, 479–481.

Cossé, J. (2010). Drag reduction due to reconfiguration. Work conducted at Ecole Polytechnique.

Dabiri, J. O. (2011). Potential order-of-magnitude enhancement of wind farm power density via counter-rotating vertical-axis wind turbine arrays. *Journal of Renewable and Sustainable Energy 3*.

Eloy, C., R. Lagrange, C. Souilliez, and L. Schouveiler (2008). Aeroelastic instability of cantilevered flexible plates in uniform flow. *Journal of Fluid Mechanics 611*, 97–106.

Etnier, S. A. and S. Vogel (2000). Reorientation of daffodil (narcissus: Amaryllidaceae) flowers in wind: Drag reduction and torsional flexibility. *American Journal of Botany*, 29–32.

Gosselin, F., E. de Langre, and B. A. Machado-Almeida (2010). Drag reduction of flexible plates by reconfiguration. *Journal of Fluid Mechanics 650*, 1–23.

Hau, E. (2006). *Wind Turbines: Fundamentals, Technologies, Applications, Economics*. Germany: Springer.

Hœpffner, J. and Y. Naka (2011). Oblique waves lift the flapping flag. *Physical Review Letters 107*.

Johnson, E. and J. D. Jacob (2009, January). Development and testing of a gust and shear tunnel for NAVs and MAVs. *47th AIAA Aerospace Sciences Meeting*.

Kim, D., J. Cossé, C. H. Cerdeira, and M. Gharib (2013, December). Flapping dynamics of an inverted flag. *Journal of Fluid Mechanics*.

Kim, D. and M. Gharib (2011). Flexibility effects on vortex formation of translating plates. *Journal of Fluid Mechanics 677*.

Kinzel, M., Q. Mulligan, and J. O. Dabiri (2012). Energy exchange in an array of vertical-axis wind turbines. *Journal of Turbulence 13*.

Kornecki, A., E. H. Dowell, and J. O'Brien (1976). On the aeroelastic instability of two-dimensional panels in uniform incompressible flow. *Journal of Sound and Vibration*, 163–178.

Luhar, M. and H. M. Nepf (2011). Flow-induced reconfiguration of buoyant and flexible aquatic vegetation. *Journal of Limnology and Oceanography*, 2003–2017.

P. Buchak, C. E. and P. M. Reis (2010, November). The clapping book: Wind-driven oscillations in a stack of elastic sheets. *Physical Review Letters 105*.

Rinaldi, S. and M. P. Paidoussis (2012). Theory and experiments on the dynamics of a free-clamped cylinder in confined axial air-flow. *Journal of Fluids and Structures 28*, 167–179.

Ristroph, L. and J. Zhang (2008). Anomalous hydrodynamic drafting of interacting flapping flags. *Physical Review Letters 101*.

Schmitz, F. W. (1941). Aerodynamics of the model airplane. Part 1. Airfoil measurements.

Sheldahl, R. E., B. F. Blackwell, and L. V. Feltz (1977). Wind tunnel performance data for two- and three-bucket Savonius rotors. *Journal of Energy 2*.

Shelley, M. J., N. Vandenberghe, and J. Zhang (2005). Heavy flags undergo spontaneous oscillations in flowing water. *Physical Review Letters 94*.

Shepherd, R. F., F. Ilievski, W. Choi, S. A. Morin, A. A. Stokes, A. D. Mazzeo, X. Chen, M. Wang, and G. M. Whitesides (2011). Multigate soft robot. *PNAS*.

Taneda, S. (1968, February). Waving motions of flags. *Journal of the Physical Society of Japan 24*, 392–401.

Tang, L., M. P. Paidoussis, and J. Jiang (2009). Cantilevered flexible plates in axial flow: Energy transfer and the concept of flutter-mill. *Journal of Sound and Vibration 326*, 263–276.

Taylor, G. W., J. R. Burns, S. M. Kammann, W. B. Powers, and T. R. Welsh (2001, October). The energy harvesting eel: A small subsurface ocean/river power generator. *IEEE Journal of Oceanic Engineering 26*, 539–547.

Vogel, S. (1984). Drag and flexibility in sessile organisms. *American Zoology 24*.

Vogel, S. (1989, August). Drag and reconfiguration of broad leaves in high winds. *The Journal of Experimental Botany 40*, 941–948.

Zhang, J., S. Childress, A. Libchaber, and M. J. Shelley (2000, December). Flexible filaments in a flowing soap film as a model for one-dimensional flags in a two-dimensional wind. *Letters to Nature 408*, 835–839.